Check for updates

JGR Earth Surface

RESEARCH ARTICLE
10.1029/2023JF007551

Special Section:
Forcing, response, and impacts of coastal storms in a changing climate

Interrelated Coastal Flooding, Erosion, and Groundwater Salinization on a Barrier Island During Hurricane Fiona

Julia A. Cantelon[1], Nicole K. LeRoux[1], Ryan P. Mulligan[2], Laura Swatridge[2], and Barret L. Kurylyk[1]

[1]Department of Civil and Resource Engineering and Centre for Water Resources Studies, Dalhousie University, Halifax, NS, Canada, [2]Department of Civil Engineering and Beaty Water Research Centre, Queen's University, Kingston, ON, Canada

Key Points:

- Morphologic and hydrogeologic monitoring captured related coastal flooding, erosion, and beach aquifer salinization following a hurricane
- High water levels drove extensive foredune scarping, which reduced island width and increased flooding and rapid seawater intrusion
- Slow recovery from dune scarping increases the landward extent of flood inundation during moderate water levels and prolongs aquifer recovery

Supporting Information:

Supporting Information may be found in the online version of this article.

Correspondence to:

J. A. Cantelon,
julia.cantelon@dal.ca

Citation:

Cantelon, J. A., LeRoux, N. K., Mulligan, R. P., Swatridge, L., & Kurylyk, B. L. (2024). Interrelated coastal flooding, erosion, and groundwater salinization on a barrier island during Hurricane Fiona. *Journal of Geophysical Research: Earth Surface*, *129*, e2023JF007551. https://doi.org/10.1029/2023JF007551

Received 20 NOV 2023
Accepted 18 MAR 2024

Author Contributions:

Conceptualization: Julia A. Cantelon, Nicole K. LeRoux, Ryan P. Mulligan, Barret L. Kurylyk
Data curation: Julia A. Cantelon, Nicole K. LeRoux, Ryan P. Mulligan, Laura Swatridge
Formal analysis: Julia A. Cantelon, Nicole K. LeRoux
Funding acquisition: Barret L. Kurylyk

© 2024. The Authors.
This is an open access article under the terms of the Creative Commons Attribution License, which permits use, distribution and reproduction in any medium, provided the original work is properly cited.

Abstract Coastal flooding transforms barrier island morphology and rapidly salinizes freshwater lenses that support island populations and ecosystems. Climate change is expected to increase coastal flood risks, and understanding future island vulnerability requires understanding erosion and salinization processes and their feedbacks. This study investigates how island morphology and groundwater salinity distributions on Hog Island, Prince Edward Island, Canada, responded to high water levels during post-tropical storm Fiona (24 September 2022), the costliest hurricane to make landfall in Canadian history. Island morphology was monitored with drone-based LiDAR, and beach groundwater dynamics were investigated with frequency-domain electromagnetic geophysics surveys and monitoring wells. Comparing pre-storm and post-disturbance data revealed high dune scarping that thinned the ocean-side foredune by 12.3 m on average and reduced the total island volume by 12%. Beach groundwater levels and electrical conductivity increased by up to 2 m and 19 mS cm^{-1}, respectively, and the freshwater lens was lost under the eroded foredune. Measurements 9 months after the storm revealed early-stage recovery of the foredune; however, high dune scarping prolonged recovery, and the island volume only increased by 1%. Without a stable ocean-side foredune, the landward extent of recurring coastal flooding increased and limited freshwater flushing and aquifer recovery. Results indicate that rapid erosion from extreme coastal storms shifts coastal boundaries, salinizes formerly freshwater resources, and limits freshwater recovery. These findings emphasize the importance of understanding the often-overlooked interconnections between coastal flooding, erosion, and groundwater salinization to effectively manage coastal resources in an age of environmental change.

Plain Language Summary Rising sea levels and more frequent storm surges will increase coastal flooding events that erode barrier island coastlines and salinize fresh groundwater. This poses a risk to economic assets, ecosystems, and potable water resources along island coasts. This study monitored changes in shoreline position and groundwater salinity following a tropical cyclone that impacted a barrier island in Prince Edward Island, Canada. Results show that high water levels and associated beach flooding drive rapid erosion and groundwater salinization. After the storm, seawater flooding increases along the eroded coastline, limiting recovery of the high-elevation dunes and groundwater freshening. Collected data show that the state of coastal dunes controls the distribution of fresh groundwater on barrier islands, and rapid erosion can have prolonged but often overlooked impacts on available freshwater. These findings have important implications for understanding and managing coastal flood risks and water security on barrier islands in a changing climate.

1. Introduction

Low-elevation coastal zones (LECZ; <10 m elevation) have abundant ecosystem services that support intense socio-economic development and dense human populations (~625 million people globally) that are on the rise (Barbier et al., 2011; McGranahan et al., 2007). Sandy coastlines make up a third of the global coastline, and their capacity to dissipate wave energy and undergo dynamic changes (erosion and accretion) in response to ocean levels (rising sea levels and storm events) provides a critical coastal defense service (Vousdoukas et al., 2020). Millions of people rely on fresh aquifers for potable water along the global coastline. However, the landward encroachment of seawater into fresh aquifers, referred to as saltwater intrusion (SWI), threatens this life-sustaining resource (Cantelon et al., 2022; Werner et al., 2013). Development, land subsidence, rising seas, flooding, and erosion are transforming coastlines at an accelerating rate, reducing the capacity for coastal protection and salinizing freshwater reserves (Michael et al., 2017; Vousdoukas et al., 2020). While a few studies have noted the connection between coastal flooding, geomorphology, and groundwater resources (e.g., Holt

21699011, 2024, 4, Downloaded from https://agupubs.onlinelibrary.wiley.com/doi/10.1029/2023JF007551, Wiley Online Library on [18/06/2024]. See the Terms and Conditions (https://onlinelibrary.wiley.com/terms-and-conditions) on Wiley Online Library for rules of use; OA articles are governed by the applicable Creative Commons License

Investigation: Julia A. Cantelon, Nicole K. LeRoux
Methodology: Julia A. Cantelon, Nicole K. LeRoux, Barret L. Kurylyk
Project administration: Nicole K. LeRoux, Barret L. Kurylyk
Resources: Ryan P. Mulligan, Laura Swatridge, Barret L. Kurylyk
Supervision: Barret L. Kurylyk
Validation: Julia A. Cantelon
Visualization: Julia A. Cantelon, Nicole K. LeRoux
Writing – original draft: Julia A. Cantelon
Writing – review & editing: Nicole K. LeRoux, Ryan P. Mulligan, Laura Swatridge, Barret L. Kurylyk

et al., 2019; Huizer et al., 2017; Schneider & Kruse, 2003, 2006), feedback between these processes is poorly understood.

Flooding, shoreline retreat, and SWI driven by changing marine conditions may disturb ecosystems, societies, and economies within the LECZ, disproportionately affecting vulnerable demographics (IPCC, 2023). Until recently, much of the work assessing processes and future vulnerabilities focused on the impacts of sea level rise (SLR) rather than extreme events (e.g., Vitousek et al., 2017). Increasingly high-resolution climate models project more frequent and intense coastal storms (Marsooli et al., 2019; Wu et al., 2022) with extreme water levels (combined tides, waves, and storm surges) and higher mean sea levels (Barnard et al., 2019; Vitousek et al., 2017; Vousdoukas et al., 2018). Together, extreme water levels and SLR may increase the population exposed to flooding by sevenfold (Barnard et al., 2019). Such estimates focus on impacts at the land surface, while *subsurface* impacts from SWI often remain "out of sight, out of mind." However, in the future, SWI driven by flooding and erosion may degrade potable water resources for millions and exceed SWI from overpumping or SLR (Holding & Allen, 2015b).

In the context of global environmental change, small ocean islands are a sentinel world region (IPCC, 2023). Over long periods (>100 years), unfortified islands can morphodynamically respond to changing marine conditions and maintain their size; however, over short periods (<100 years), morphodynamic changes in response to extreme events can result in unstable shorelines that are vulnerable to coastal flooding and SWI or, in extreme cases, island submergence (Durán Vinent & Moore, 2015; Ghosh et al., 2014; McNamara & Lazarus, 2018). Small-island populations and economic assets are predominantly within the LECZ; consequently, floods and erosion can impact infrastructure, potable water supply, and salt-intolerant crops. Furthermore, small islands are uniquely susceptible to water insecurity and climate disasters due to their size, remoteness, limited resource base, and hazard exposure. Between 1997 and 2018, small island developing states experienced a 78% increase in water and climate disasters (Gheuens et al., 2019). Local stakeholders often focus on surface impacts (loss of lives and infrastructure) that directly displace island inhabitants (Ghosh et al., 2014); however, SWI from coastal storms poses an additional environmental hazard as it can degrade drinking water resources and habitats forcing islands to adopt expensive alternatives or migrate (Gheuens et al., 2019; IPCC, 2023; Storlazzi et al., 2018). Recent summaries have found that over 90% of low-lying, small-island developing states are at risk of water scarcity (UNESCO-IHP & UNEP, 2016) and have called for increasing attention given global climate change risks (Hay, 2013; Holding et al., 2016; Robins, 2013).

In the absence of surface water, island potable freshwater is limited to a thin, fresh aquifer known as a freshwater lens that forms when fresh precipitation infiltrates and "floats" above denser saline groundwater. Freshwater scarcity concerns small-island populations as a small decrease in water-table elevation relative to sea level causes the freshwater lens to vertically contract by ~40 times the water table drop (Ghyben, 1888; Herzberg, 1901). Such changes can occur in response to groundwater pumping (Bryan et al., 2016), climate variations (precipitation and evapotranspiration; Briggs et al., 2021; Holding& Allen, 2015a), ocean levels (sea levels, tides, surge, waves; Anderson, 2002; Ataie-Ashtiani et al., 1999, 2013), and changes in island geomorphology (Chesnaux et al., 2021; Huizer et al., 2017; Schneider & Kruse, 2003). Further, climatic, oceanic, and morphologic drivers interact; for example, changes in morphology can impact the area for fresh recharge (Zhang et al., 2016) or the inundation of land with seawater (Stanic et al., 2024; Yu et al., 2016). However, most studies have assessed drivers in isolation, and few have considered the co-evolution of morphology and fresh groundwater resources.

For coastal communities, particularly islands, water security and disaster risk reduction rely on understanding dynamics to plan short-term mitigation and long-term adaptation strategies (Toimil et al., 2020). Understanding how flooding and erosion drive freshwater loss is important for future freshwater security and requires multidisciplinary research. Coastal geomorphologists have made significant progress in understanding shoreline movements in response to storms and interannual climate variability (Hesp & Walker, 2022; Houser et al., 2008; Mathew et al., 2010). Meanwhile, advances in groundwater monitoring and numerical modeling have allowed coastal hydrogeologists to investigate coastal groundwater dynamics, including the effects of coastal flooding (Elsayed & Oumeraci, 2018; Oberle et al., 2017; Post & Houben, 2017), gradual shoreline transgressions (Holt et al., 2019; Schneider & Kruse, 2006; Stanic et al., 2024), and anthropogenic nourishment and excavation (Briggs et al., 2021; Huizer et al., 2016) on aquifer salinity distributions. However, research assessing how rapid shoreline retreat during coastal storms impacts aquifer salinity remains limited as traditional monitoring infrastructure is often damaged or lost during storms, and inflexible groundwater model domains limit numerical

21699011, 2024, 4, Downloaded from https://agupubs.onlinelibrary.wiley.com/doi/10.1029/2023JF007551, Wiley Online Library on [18/06/2024]. See the Terms and Conditions (https://onlinelibrary.wiley.com/terms-and-conditions) on Wiley Online Library for rules of use; OA articles are governed by the applicable Creative Commons License

simulations of these coupled surface-subsurface processes. As such, there is a gap in understanding how coastal flooding, erosion, and SWI processes interact. This study aims to address this knowledge gap by investigating erosion and SWI wrought by Hurricane Fiona (24 September 2022) on an uninhabited barrier island in Prince Edward Island (PEI), Canada. Between September 2022 and May 2023, field campaigns were performed to assess pre-disturbance, post-disturbance, and early recovery morphology with LiDAR and groundwater salinity distributions recorded in 3D with electromagnetic geophysics and monitoring wells. Pre- and post-disturbance data were compared to quantify dune erosion and SWI, and post-disturbance and early recovery (9 months) data were compared to quantify morphologic recovery and aquifer freshening. Results from this natural setting provide new insights into the connection between oceanic forcing, barrier island morphodynamics, and freshwater resources and processes that drive SWI in an era of rising seas and intensifying ocean storms. Process-based SWI understanding from this work will help deconvolute oceanic and anthropogenic forcings on populated islands to inform management plans that holistically consider interrelated stressors.

2. Materials and Methods

2.1. Field Site Description

The northwest shore of PEI, Canada, has been an essential part of the Mi'kmaq traditional territory for thousands of years and is currently a hot spot for economic activity, including agriculture, aquiculture, commercial fisheries, recreation, and tourism (Figure 1b; Vasseur & Catto, 2008). Just offshore, a series of long, narrow, sand barrier islands (43 km total length) run parallel to mainland PEI (southeast-northwest), separating the shallow waters of Malpeque and Cascumpec Bays from the Gulf of St. Lawrence (Figure 1c). The barrier island chain is one of the most important coastal dune ecosystems in eastern Canada for its role in protecting estuaries, coastlines, and Mi'kmaq heritage tied to this land (Parks Canada, 2021). However, erosion (0.26 m year^{-1} between 1935 and 1977) threatens the future of these thin (<1 km) islands (Armon & McCann, 1977). Lennox Island, located in Malpeque Bay (Figure 1c) on the landward side of the barrier island chain, is the home of the Lennox Island Mi'kmaq First Nation. This island is composed of highly erodible sandstone, and despite low wave heights in Malpeque Bay due to the barrier islands (Figure 1b), the area of Lennox Island decreased by 18% between 1880 and 2010 driven by rising sea levels and winter wave action intensification (Dietz & Arnold, 2021; MacDonald, 2014). Erosion is an ongoing threat to the Lennox Island Mi'kmaq First Nation's fresh groundwater, infrastructure, archeological records, history, and culture and is a somber reminder of the critical role that barrier islands play in protecting sentinel coastal zones (Stanic et al., 2024). To preserve Mi'kmaq cultural land use traditions, ecological integrity, and ecosystem services tied to this barrier island chain, the Mi'kmaq of PEI and Parks Canada established Pituamkek ("At the long sand dune"), herein referred to as Hog Island, as a Canadian National Park Reserve (Parks Canada, 2021).

Hog Island, PEI (46.63°N, 63.83°W) is a long, narrow island (14 km alongshore and 0.3–1.2 km cross-shore) and is the largest island in the Malpeque barrier island system (Figure 1c). The island has a high (5–15 m above mean sea level; aMSL) dune ridge composed of well-sorted, medium to fine sand (d_{50} = 0.28 mm) that overlies Permo-Carboniferous sandstone bedrock ∼10 m below mean sea level (bMSL). Multiple blowouts and washover fans fragment the dune ridge, and numerous tidal inlets have fragmented the island and gradually filled it (Figure 1c; Armon, 1980; Dolan, 2022). The north shore (Gulf of St. Lawrence) of Hog Island is a wide unvegetated beach with a steep and sparsely vegetated foredune. In contrast, the south backslope (Malpeque Bay) has a gradual slope and denser vegetation (Figure 1c). The island has no infrastructure except a small weather station (ID: Hog Island, 20599512; MCPEI, 2023) maintained by the University of PEI and the Mi'kmaq Confederacy of PEI. Weather station data reveal that the island has mild summers (average air temperature 21°C in 2022) and cool winters (average −2.9°C in 2022) and receives 1,050 mm of precipitation evenly distributed throughout the year (Figure S1 in Supporting Information S1). Without fresh surface water bodies, a freshwater lens sustains the vegetation (dune grass, shrubs, and trees) that provides habitats for foxes, endangered bats, and seabirds (Parks Canada, 2021). Hog Island is presently uninhabited by humans, and no groundwater pumping occurs, making it an ideal observatory to study ocean-aquifer interactions in isolation from anthropogenic influences (development, coastal fortification, and pumping).

The north shore of PEI has high rates of relative sea-level rise (approximate rate of 3.2 mm/year from 1911 to 2020) from glacial isostatic adjustment and anthropogenic climate change (Holgate et al., 2013). The tides are mixed, mainly semi-diurnal, with a micro-tidal range (0.45–1.0 m neap-spring). Significant wave heights (H_s) are

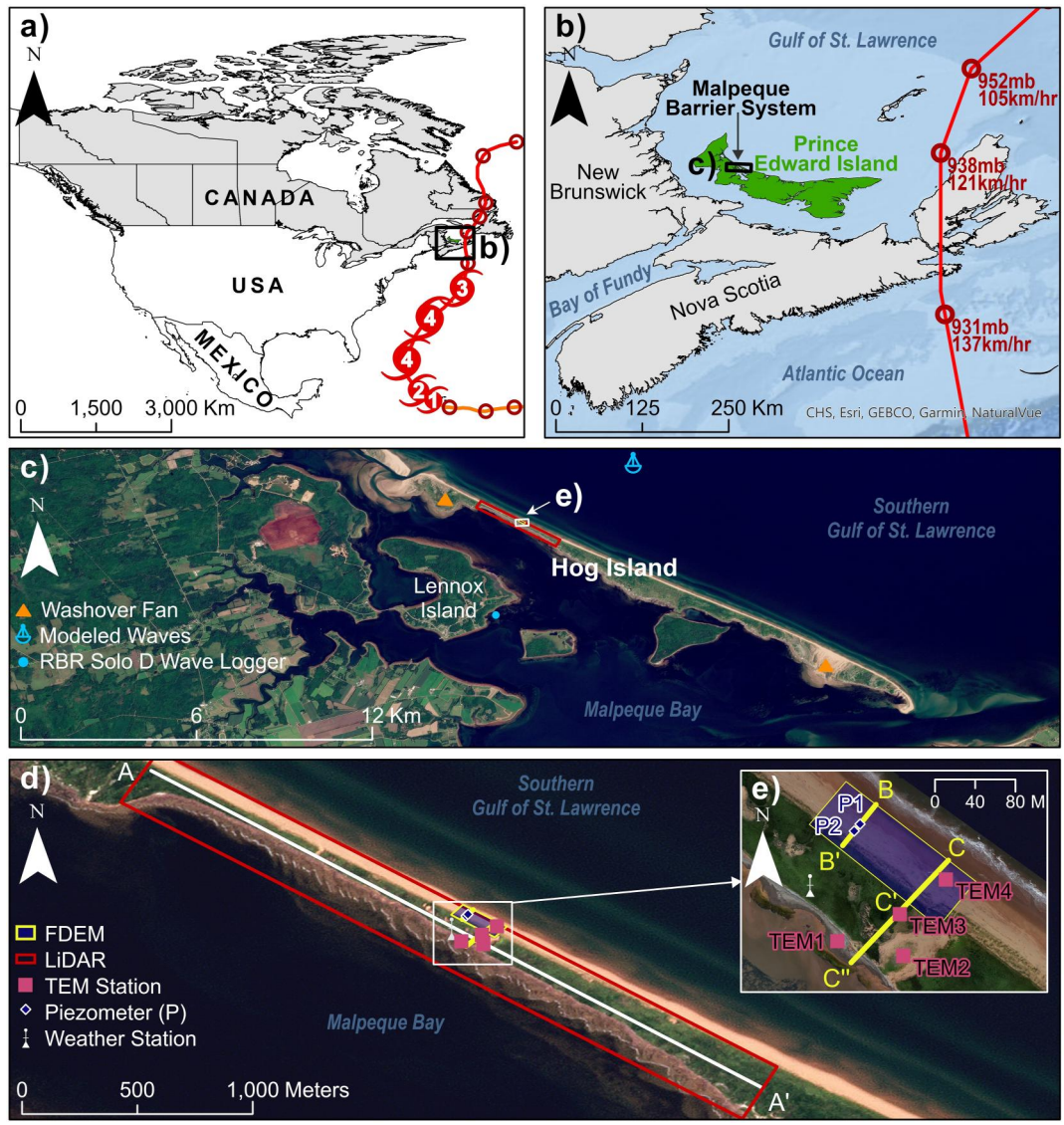

Figure 1. Maps showing (a) the track of Hurricane Fiona (data from Pasch et al. (2023)) between 14 and 24 September 2022, as it developed into a category four hurricane, and (b) made landfall in Atlantic Canada as a post-tropical storm passing 200 km east of the Malpeque Barrier system in Prince Edward Island, Canada. Labels show the minimum sea-level pressure and maximum surface wind speed data at 6-hr intervals from Pasch et al. (2023). (c) Locations of Hog and Lennox Islands, washover fans, and wave data hindcasting node. (d) Drone-based LiDAR, time-domain and frequency-domain electromagnetic geophysics survey footprints, and (e) piezometer, climate station, and geophysics monitoring transects. Background satellite imagery from Planet Team (2017).

generally low in the Gulf of St. Lawrence as it is a protected, shallow sea (<200 km fetch, 40–60 m depth). Analysis of 65 years of hindcasted wave data from 3 km offshore of Hog Island (~30 m depth) reveals that waves are predominantly from the northwest and have a mean significant wave height of 0.59 m and a period of 3.7 s (Figure S2 in Supporting Information S1; DFO, 2023). Mean significant wave heights in the winter (December-February; $H_s = 1.14$ m) are higher than spring (March-May; $H_s = 0.3$ m), summer (June-August; $H_s = 0.4$ m), and fall (September-November; $H_s = 0.6$ m) (Figure S3; DFO, 2023). The average wind speed on Hog Island is 6.6 m s^{-1}, predominantly from the southwest, while the strongest winds (>15 m s^{-1}) tend to come from the northwest between October and April (Figure S1 in Supporting Information S1). In the winter, sea ice covers up to 20% of Malpeque Bay and moderates wave action; however, the area of winter ice cover has decreased in recent years (Dolan, 2022; Jardine, 2022).

21699011, 2024, 4, Downloaded from https://agupubs.onlinelibrary.wiley.com/doi/10.1029/2023JF007551, Wiley Online Library on [18/06/2024]. See the Terms and Conditions (https://onlinelibrary.wiley.com/terms-and-conditions) on Wiley Online Library for rules of use; OA articles are governed by the applicable Creative Commons License

21699011, 2024, 4, Downloaded from https://agupubs.onlinelibrary.wiley.com/doi/10.1029/2023JF007551, Wiley Online Library on [18/06/2024]. See the Terms and Conditions (https://onlinelibrary.wiley.com/terms-and-conditions) on Wiley Online Library for rules of use; OA articles are governed by the applicable Creative Commons License

Hydrodynamic and climate data explain alongshore trends in the morphology of Hog Island. Subtidal and supratidal sediment inputs from shoreface erosion contribute to high alongshore sediment transport rates (500–2,000 $m^3\ yr^{-1}$) that increase toward the southeast (Armon & McCann, 1977; Davies, 2011). Alongshore sediment transport from west to east causes the island to migrate eastward (Armon, 1980; McCann, 1972). Hog Island has generally maintained its width via gradual backslope accretion from aeolian sediment transport and wave-driven recession on the ocean side (Armon & McCann, 1979; Dolan, 2022). However, transgression rates are low as high dunes and low wave heights prevent frequent or extensive overwash and sediment transport. Recent trends suggest that Hog Island is narrowing and increasingly susceptible to erosion, particularly in the northwest where monitoring was focused (Figure 1c).

2.2. Landfall of Hurricane Fiona in Atlantic Canada

Hurricane Fiona weakened over the cool waters in Atlantic Canada (Figures 1a and 1b) and entered the Gulf of St. Lawrence as a strong post-tropical storm. Parts of Nova Scotia and Newfoundland measured hurricane-force wind gusts and a minimum atmospheric pressure of 93.2 kPa, a record low in Atlantic Canada (Pasch et al., 2023). The Hog Island weather station recorded a minimum atmospheric pressure of 97.1 kPa and strong wind gusts (up to 30.2 m s^{-1}) from the north (Figure 2a). Mulligan et al. (2023) simulated ocean levels during Hurricane Fiona, and their model results indicate that there was a 1.3 m storm surge in the Gulf of St. Lawrence north of Hog Island (location in Figure 1c). Further modeling results suggest that large waves with maximum significant wave heights of 4.5 m battered the north shore (Figures 2c and 2d). Monitoring in Malpeque Bay with an RBRsoloD wave logger sampling at 16 Hz revealed a maximum storm surge of 1.8 m and small waves with significant wave heights <0.2 m (Figures 2c and 2d).

Extreme value analysis (Figure S2b in Supporting Information S1; Kamphuis, 2020) on 65 years of hindcast wave data for the modeled location revealed that the maximum significant wave heights observed during this storm have a relatively short return period (<3 years). However, water levels from the combined effect of waves and storm surge made this a historic event, significantly impacting coastal developments and ecosystems in PEI (e.g., Bonnington et al., 2023). Satellite imagery from Planet Team (2017) and images from the COASTIE citizen science program (coastiecanada.ca) revealed intensive beach/dune erosion and sediment transport (Figure 3b). Globally, damages from Hurricane Fiona were estimated to be $3.09 billion (USD), and insured losses in Atlantic Canada were $800 million, making it the costliest weather event to impact Atlantic Canada and the seventh most expensive in Canadian history (Pasch et al., 2023).

2.3. Field Data Collection

Between 2020 and 2021, repeated field campaigns were conducted to monitor nearshore hydrodynamics, morphology, and fresh groundwater resources along a narrow 3.1-km stretch of northeast Hog Island (Dolan, 2022). This study reports on three repeat field campaigns between September 2022 and May 2023 that monitored island morphology with drone-based LiDAR and ground-based differential GPS (DGPS) surveys and groundwater dynamics with electromagnetic geophysics surveys, two piezometers, and pits dug to the water table (Figure 1d). Field data collected on 6 October 2022 (post-disturbance) were compared to pre-disturbance data collected 19 September 2022 to quantify erosion and SWI on Hog Island due to Hurricane Fiona on 24 September 2022 (Figures 1a and 3c–3f). On 25 May 2023, a third survey (recovery) was performed, and data were compared to the post-disturbance survey to assess early stage morphologic recovery and aquifer flushing. The piezometer data record was limited (pre-disturbance to post-disturbance) as piezometer standpipes were damaged in the storm (see Section 2.3.2 for details). During the recovery survey, pits were dug to the water table to survey the beach groundwater in the absence of piezometers. Other data sources include satellite imagery (Planet Team, 2017), hindcast wave data (DFO, 2023), ocean water levels and significant wave heights modeled by Mulligan et al. (2023), bay water levels and wave heights recorded with an RBRSolo D wave logger, and meteorological measurements from the climate station (MCPEI, 2023).

2.3.1. Morphologic Monitoring

Drone-based LiDAR surveys were conducted using a DJI Matrice 300 RTK drone with a DJI Zenmuse L1 LiDAR sensor capable of recording RGB photographs. LiDAR surveys of a 0.6 km^2 area (3.1 km alongshore) were flown 100 m above MSL at a speed of 7 m s^{-1} (Figure 1d), with manufacturer-reported vertical and horizontal

21699011, 2024, 4, Downloaded from https://agupubs.onlinelibrary.wiley.com/doi/10.1029/2023JF007551, Wiley Online Library on [18/06/2024]. See the Terms and Conditions (https://onlinelibrary.wiley.com/terms-and-conditions) on Wiley Online Library for rules of use; OA articles are governed by the applicable Creative Commons License

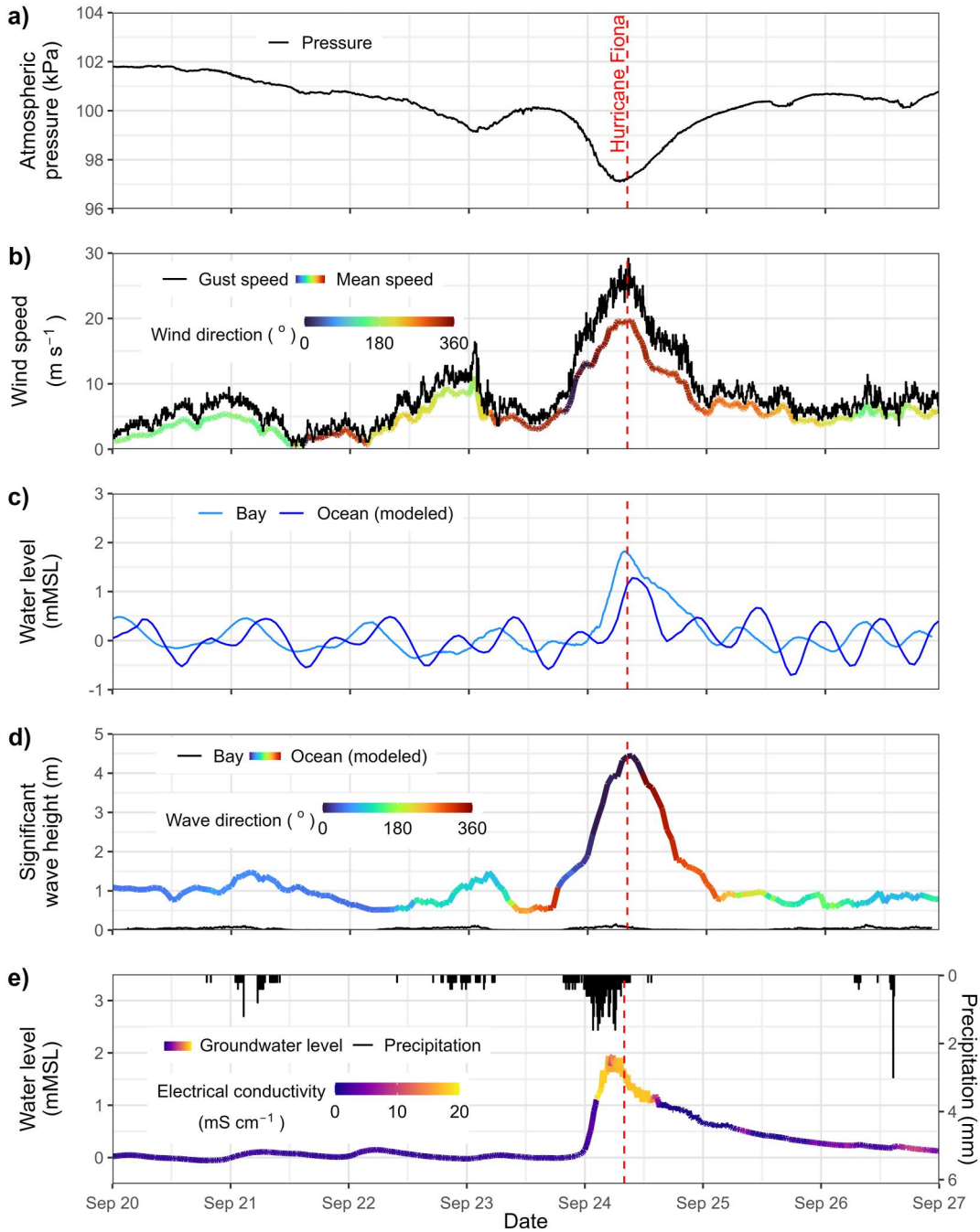

Figure 2. Time series (Atlantic Daylight Time) of meteorologic, oceanographic, and hydrogeologic conditions on Hog Island, Prince Edward Island, between 20 and 27 September 2022, with Hurricane Fiona passing on 24 September 2022. Meteorological data include (a) atmospheric pressure and (b) wind gust speed, mean speed, and direction (° from North) observed at the Hog Island climate station (ID: Hog Island, 20599512; MCPEI, 2023). (c) Water levels, (d) significant wave heights, and the dominant wave direction (° from North) recorded in the Malpeque Bay wave logger and modeled in the Gulf of St. Lawrence (see Figure 1c for locations). (e) Groundwater level and electrical conductivity at piezometer P2 (Figure 1d) and precipitation recorded at the climate station.

accuracies of 5 and 10 cm, respectively, when flown at 50 m. High spatial resolution data (480,000 points s^{-1}) were collected in the WGS84 UTM Zone 20N horizontal coordinate system relative to the standard Canadian geodetic vertical datum (CGVD 2013a). Horizontal coordinate data were projected to NAD83 (CSRS) UTM Zone 20N for analysis. All surveys were performed at low tidal stages using identical settings and flight paths.

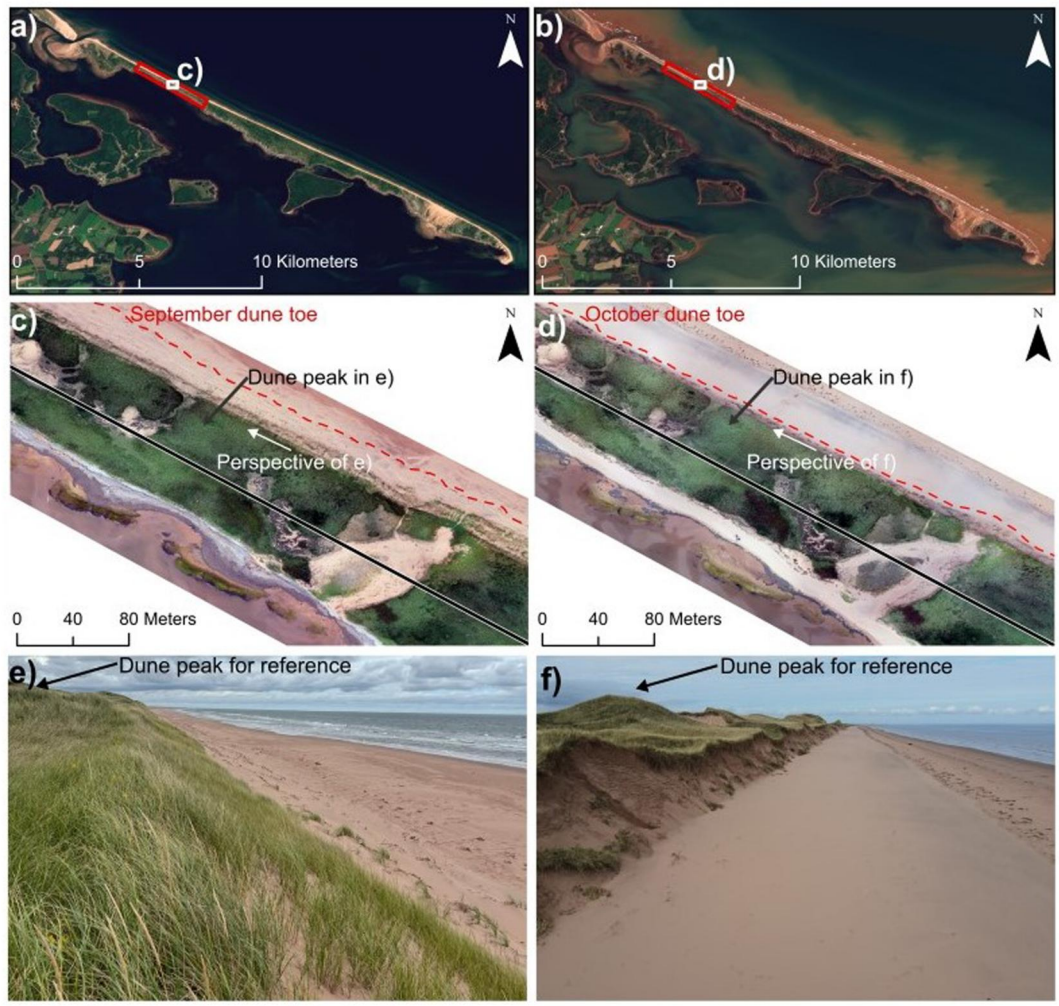

Figure 3. Planet satellite imagery (Planet Team, 2017) shows Hog Island (a) before (4 September 2022) and (b) after (25 September 2022) the landfall of Hurricane Fiona on 24 September 2022. Orthomosaics from (c) pre-disturbance (20 September 2022) and (d) post-disturbance (6 October 2022) drone surveys in the FDEM survey area. Images taken during the (e) pre-disturbance and (f) post-disturbance surveys showing the same perspective of the dune line following the storm. The red rectangles depict the footprint of the 0.6 km^2 drone-based LiDAR surveys, and the red dashed line shows the north dune toe.

Raw LiDAR surveys were imported into DJI Terra (DJI, Shenzhen, China) to construct 3D models from point cloud data. Point cloud 3D models generated in DJI Terra were ground-classified and converted to digital elevation models (DEMs) with 0.1×0.1 m cells in ArcGIS Pro (ESRI, Ontario, Canada). RGB imagery was used to generate visual orthomosaics (Figures 3c and 3d, Figure S4 in Supporting Information S1) in Pix4Dmapper (Pix4D, Prilly, Switzerland) with a 0.03 m resolution to qualitatively assess changes in island morphology and land cover. Ground control points (GCPs) were collected at 36 locations across the foreshore, backshore, and dune using a DGPS with a vertical and horizontal accuracy of 0.14 and 0.07 cm, respectively (Emlid Reach RS2). The mean root mean square error between surface elevations derived with drone-based LiDAR and the DGPS at GCPs was 0.31 and 0.32 m for the October 2022 and May 2023 surveys, respectively (Figure S5 in Supporting Information S1). This error is similar to the combined instrument errors and comparable to errors obtained in a coastal study using similar settings and flight conditions for the L1 LiDAR sensor with the Matrice 300 RTK drone (LeRoux et al., 2024).

For each survey, alongshore parameter extraction was performed every 1 m along the A-A' transect to derive the position and elevation of the north (Gulf of St. Lawrence) and south (Malpeque Bay) shoreline, dune toe, and dune crest (Figure 1d). The north and south shorelines (low-tide water line) were visually interpreted for each survey

21699011, 2024, 4, Downloaded from https://agupubs.onlinelibrary.wiley.com/doi/10.1029/2023JF007551, Wiley Online Library on [18/06/2024]. See the Terms and Conditions (https://onlinelibrary.wiley.com/terms-and-conditions) on Wiley Online Library for rules of use; OA articles are governed by the applicable Creative Commons License

21699011, 2024, 4, Downloaded from https://agupubs.onlinelibrary.wiley.com/doi/10.1029/2023JF007551, Wiley Online Library on [18/06/2024]. See the Terms and Conditions (https://onlinelibrary.wiley.com/terms-and-conditions) on Wiley Online Library for rules of use; OA articles are governed by the applicable Creative Commons License

from high-resolution orthomosaics. The relative relief foredune parameter extraction method (Wernette et al., 2016) was used to quantify the topographic position of each DEM pixel relative to adjacent pixels and establish thresholds to extract dune toe and crest boundaries reliably. For pre-disturbance, post-disturbance, and early recovery DEMs, the relative relief of each pixel within 5, 10, 15, and 20 m windows was calculated using Equation 2 of Wernette et al. (2016). Small windows were sensitive to localized topographic variations, whereas large windows detected dominant topographic features. To increase the strength of the topographic signal relative to noise, relative relief results from each window were averaged, after which amplified landscape signals were apparent and consistent among surveys. Based on the histograms of the final average relative relief layers, multiple thresholds were tested for the automated feature (dune toe and dune crest) extraction. Ultimately, threshold values of 0.2 (dune toe) and 0.75 (crest) were the most consistent in reproducing the variation in topographic features alongshore and between surveys. Transects every 1 m along A-A' were used for automated feature extraction that detected the first position landward of the shoreline above the relative relief threshold established for the dune toe and dune crest (Figure 1d). Using the extracted positions, the south and north beach width, beach slope, beach volume, dune height, dune slope, dune volume, and total island volume (relative to MSL) were calculated following the definitions presented in Table S1 in Supporting Information S1 that are modified from George et al. (2021). To quantify morphologic change over the erosion (post-disturbance minus pre-disturbance) and recovery (early recovery minus post-disturbance) periods, DEMs and alongshore parameters were compared. Automated feature extraction results from the bay-side of Hog Island are not presented, as groundwater monitoring, dominant morphologic features, and disturbances from Hurricane Fiona were predominantly on the ocean-side. Hereafter, unless otherwise specified, the terms beach and foredune refer to the north shore (ocean side).

2.3.2. Shallow Groundwater Monitoring

The electrical conductivity (EC) zonation of the shallow groundwater was mapped using time-domain (TEM) and frequency-domain (FDEM) electromagnetic (EM) geophysical surveys. EM geophysics is commonly employed in hydrogeology and well suited for coastal applications monitoring groundwater and SWI, as the non-invasive surveys can be collected rapidly, do not require permanent installations vulnerable to erosion or burial events, and yield spatiotemporally distributed data when repeat surveys are performed (Kirsh, 2009). EM techniques capture the response of the subsurface to primary (applied) and secondary (eddy currents from the subsurface) EM fields, and inverting EM data yields the subsurface bulk resistivity (Ω m) that highlights the contrasts between high-resistivity freshwater (>30 Ω m) and low-resistivity saline water (<0.3 Ω m), particularly in homogenous geologic settings like Hog Island. Jiao and Post (2019) and Kirsh (2009) include comprehensive reviews of the operating principles and logistics of TEM and FDEM methods for mapping groundwater salinity.

TEM and FDEM data collected during a reconnaissance campaign in August 2021 revealed that the maximum depth of investigation of FDEM data (1.4–10 m) was expectedly shallow compared to TEM data (36–53 m) but was sufficient to map the fresh, brackish, and saline groundwater on the beaches of Hog Island. Further, although TEM and FDEM results were similar, the high-resolution FDEM data better resolved the transition zone dimensions than the TEM data. All subsequent surveys (pre-disturbance, post-disturbance, and recovery) only applied FDEM geophysics and direct monitoring techniques on the north beach. The Supporting Information S1 (Text S1) details the TEM methods and results that mapped groundwater at depth.

To monitor the shallow fresh and saline groundwater distribution along the north beach of Hog Island, a GEM-2 (GEOPHEX, Inc., North Carolina, USA) was used to collect multi-frequency EM data. In contrast with the cumbersome TEM instrument that takes 1D measurements, the portable GEM-2 could effectively collect 3D data at a walking pace, making it suitable for surveying a relatively large area during rapid, time-limited deployments before and after storms. FDEM data were collected at five frequencies (450, 1,530, 5,310, 18,220, 63,030 Hz) while holding the GEM-2 (fixed coil separation of 1.66 m) 1 m above the land surface in horizontal coplanar mode. Raw quadrature data were processed in the GCM module of Aarhus Workbench (Aarhus Geosoftware, 2023) by manually removing negative data points and outliers impacted by noise and inverting the data over a 3-m moving window with the AarhusInv code. Smooth 1D models of bulk resistivity with 10 layers were within a 10% relative standard deviation of the raw data. For each model, the maximum depth of investigation was the depth at which the signal crossed the background noise level. Land surface elevations derived from drone-based DEMs were applied as the surface boundary of the resulting 1D bulk-resistivity models in Leapfrog (Seequent, Pennsylvania, USA) to create a model of bulk resistivity suitable for automated alongshore feature extraction and volume calculations.

21699011, 2024, 4, Downloaded from https://agupubs.onlinelibrary.wiley.com/doi/10.1029/2023JF007551, Wiley Online Library on [18/06/2024]. See the Terms and Conditions (https://onlinelibrary.wiley.com/terms-and-conditions) on Wiley Online Library for rules of use; OA articles are governed by the applicable Creative Commons License

Bulk-resistivity data obtained from the inversion of TEM and FDEM data represent sediment and porewater electrical properties. Archie's (1942) Law was applied to estimate the saturated zone (bMSL) porewater EC from bulk-resistivity data using geologic characteristics, including the effective porosity (0.3 from sediment samples) and cementation exponent (1.3 for sand). Groundwater EC thresholds from Jiao and Post (2019) were used to delineate zones of fresh (<1.6 mS cm^{-1}), brackish (1.6–16 mS cm^{-1}), and saline (>16 mS cm^{-1}) groundwater in each survey. The north shoreline and dune toe positions derived from the pre-disturbance LiDAR survey (Section 2.3.1) were subset to the FDEM survey area (Figure 1e). At the position of the post-disturbance ocean-side (north) dune toe, the depths (relative to MSL) of the transition zone top and bottom were extracted from inverted FDEM results using the previously noted thresholds for fresh and saline groundwater. In the absence of continuous water table elevation data, the saturated zone was assumed to begin at MSL given the high hydraulic conductivity and low hydraulic gradients on Hog Island. Along 1-m wide cross-shore transects within the FDEM survey area, the volumes of fresh and brackish groundwater between the post-disturbance shoreline and the dune toe were calculated, accounting for beach sediment porosity. Fresh and brackish groundwater volumes for each survey were compared to quantify SWI (post-disturbance minus pre-disturbance) and flushing (recovery minus post-disturbance) between surveys. The post-disturbance north shoreline and dune toe were used to extract the transition zone dimensions and beach groundwater volumes from all three FDEM surveys to maintain consistent dimensions compatible for direct comparison.

To assess freshwater lens dimensions interpreted from EM results, the sharp-interface Ghyben-Herzberg relation was applied to water table elevations surveyed with a DGPS, assuming a density ratio of approximately 37 based on standard densities of freshwater (1,000 kg m^{-3}) and seawater (1,027 kg m^{-3}; Ghyben, 1888; Herzberg, 1901; Nayar et al., 2016). In addition, the Fetter (1972) analytical solution for strip-island lenses was applied using island widths derived from LiDAR data, hydraulic conductivities estimated from sand samples, and recharge rates calculated from climate data. The hydraulic conductivity of the aquifer on Hog Island was determined using falling head tests performed on sand samples taken from the north (3.4×10^{-4} m s^{-1}) and south (2.7×10^{-4} m s^{-1}) beaches and Neilsen's (1990) analytical solution for tidal signal propagation in unconfined aquifers applied to tidal groundwater level time series from north beach piezometers (4.5×10^{-4} m s^{-1}). Annual aquifer recharge (0.4 m, annual precipitation minus annual evapotranspiration) was estimated following Allen et al. (1998; Figure S1 in Supporting Information S1).

To complement EM geophysical data (spatially distributed, temporally discrete), shallow piezometers were installed on the north beach to collect time-series level and EC data (spatially discrete, temporally distributed) in the beach aquifer. Shallow piezometers (Figure 1e) collected in situ groundwater data to quantify the impacts of climatic and hydrodynamic forcing. Piezometers 1 (P1) and 2 (P2) were installed in manually augured pilot holes 26 and 35 m landward of the pre-disturbance shoreline, respectively, and backfilled with native beach sand. The land surface and top of casing elevations were surveyed with a DGPS, and the centers of the 0.3 m screened intervals of P1 and P2 were 0.3 and 0.43 m bMSL, respectively. Piezometer data were collected at 10-min intervals using Solinst conductivity, temperature, and depth (CTD) loggers. Level data were atmospherically corrected with barometric pressure data from the nearby weather station and reported relative to CGVD2013a. P2 logged data from 19 July 2022 to 6 October 2022, while P1 only logged data from 19 July 2022 to 19 September 2022, as the logger could not be recovered post-disturbance. During the May 2023 survey, pits were dug to the water table at the approximate locations of P1 and P2 and the elevation and EC of groundwater were surveyed with a DGPS and handheld probe (YSI ProDSS), respectively.

3. Results and Discussion

3.1. Pre-Disturbance Monitoring and Characterization

3.1.1. Island Morphology

Orthomosaic images derived from drone-based LiDAR on 20 September 2022 portrayed a low-elevation barrier island with variable morphology (Figure 3c, Figure S4a in Supporting Information S1). Before Hurricane Fiona, the beach was 20–41 m wide, had a low slope (mean ± standard deviation = 2.3° ± 0.5°), and was covered with vegetation and debris (Figure 3, Figures S6a, S6b, S7a, and S7b in Supporting Information S1). The dune crest elevation varied between 5.3 and 15 m aMSL (8.6 ± 1.9 m aMSL), and lower dune heights were observed in the center (1,000–1,450 m alongshore) and northwest (<500 m alongshore) portions of the A-A' transect, where the island is thin, and blowouts cause sharp decreases in the dune height (Figure 3c, Figure S6e in Supporting

Table 1
Summary of Morphologic Characteristics and the Percent Change Between Surveys

Survey	North beach width (m)	North beach volume ($m^3\ m^{-1}$)	North dune slope (°)	Island dune width (m)	North dune volume ($m^3\ m^{-1}$)	Island volume ($m^3\ m^{-1}$)	Total volume (m^3)
Pre-disturbance (1)	29 ± 3.6	18 ± 3.5	18 ± 2.9	108 ± 42	99 ± 49	537 ± 129	1.15×10^6
Post-disturbance (2)	45 ± 3.5	40 ± 4.9	29 ± 6.3	95 ± 39	47 ± 22	472 ± 124	1.01×10^6
Recovery (3)	30 ± 3.9	15 ± 5.2	17 ± 5.1	106 ± 38	58 ± 37	473 ± 121	1.02×10^6
Percent change							
(2)–(1)	55%	127%	60%	−12%	−54%	−12%	−12%
(3)–(2)	−33%	−64%	−39%	12%	23%	<1%	<1%
(3)–(1)	3%	−18%	−2%	−2%	−43%	−12%	−11%

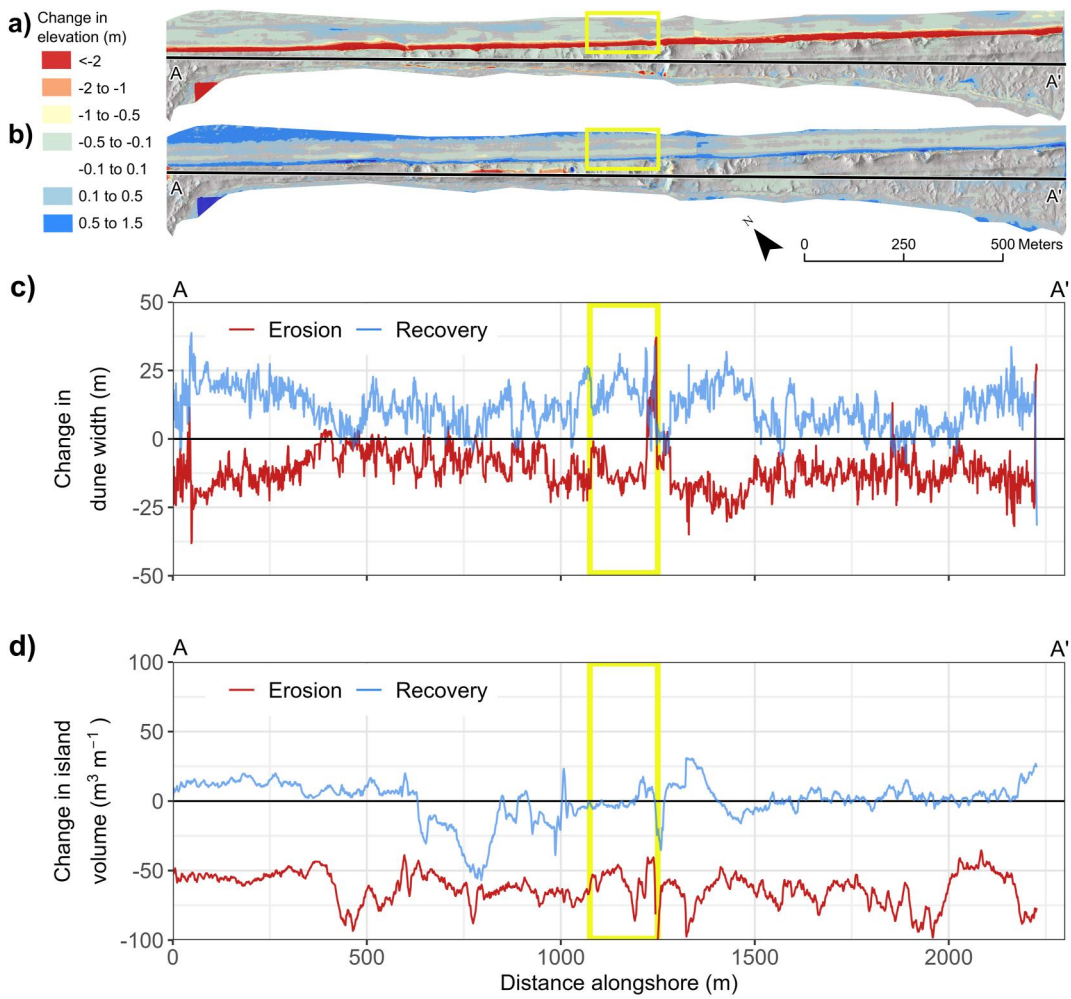

Figure 4. Change in island elevation (m) between LiDAR-generated digital elevation models over the (a) erosion and (b) recovery period. Change in (c) dune width (ocean-side to bay-side dune toe; m) and (d) island volume ($m^3\ m^{-1}$) over the erosion and recovery periods with distance on the A-A' alongshore transect (Figure 1d). The erosion period is the post-disturbance survey minus the pre-disturbance survey, and the recovery period is the recovery survey minus the post-disturbance survey. The yellow rectangle corresponds to the FDEM survey area.

21699011, 2024, 4, Downloaded from https://agupubs.onlinelibrary.wiley.com/doi/10.1029/2023JF007551, Wiley Online Library on [18/06/2024]. See the Terms and Conditions (https://onlinelibrary.wiley.com/terms-and-conditions) on Wiley Online Library for rules of use; OA articles are governed by the applicable Creative Commons License

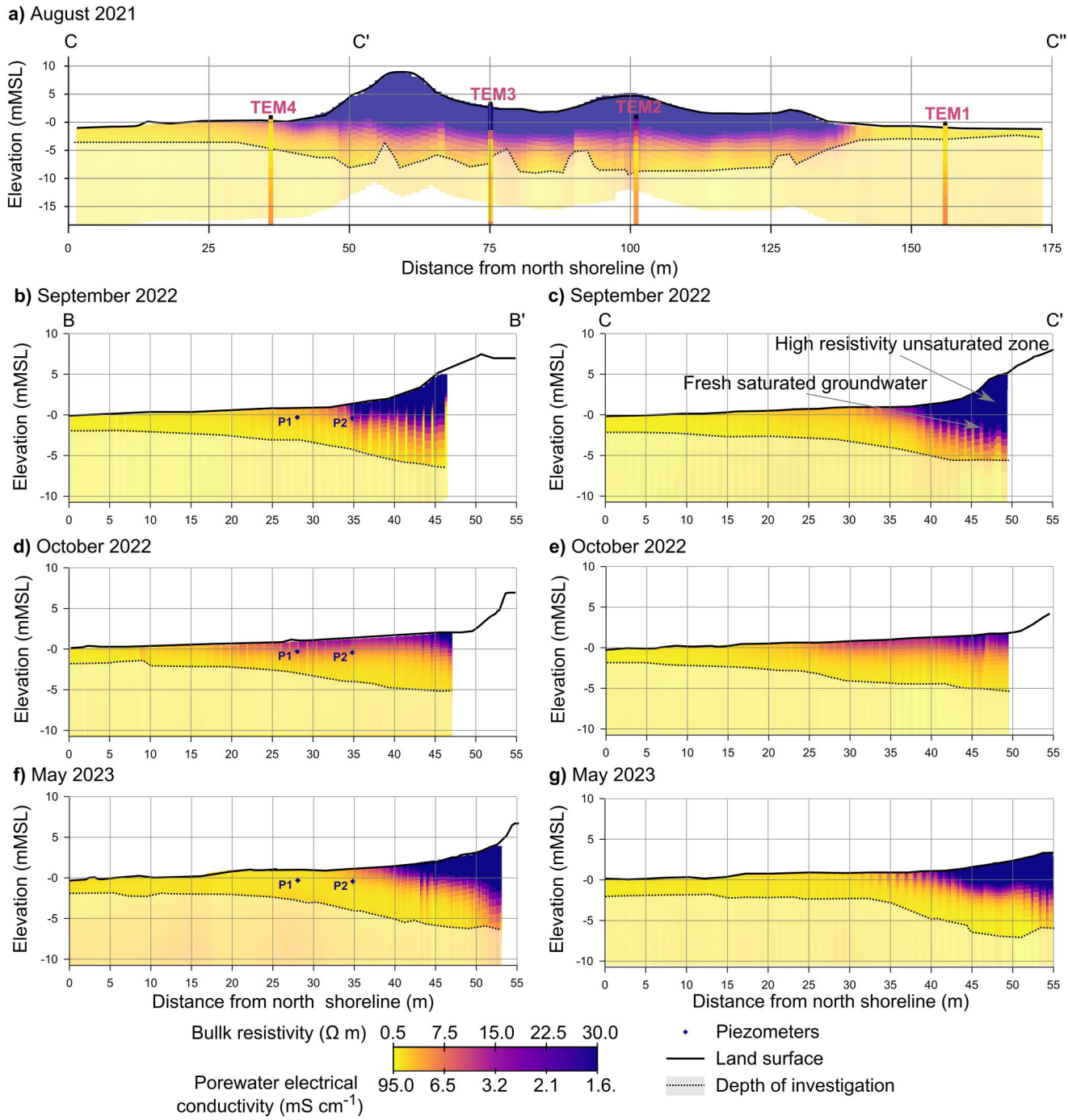

Figure 5. Inverted bulk resistivity and saturated porewater electrical conductivity from TEM and FDEM data collected in (a) August 2021 along the C-C'' transect, September 2022 (pre-disturbance) along the (b) B-B' and (c) C-C' transects, October 2022 (post-disturbance) along the (d) B-B' and (e) C-C' transects, and May 2023 (recovery) along the (f) B-B' and (g) C-C' transects (see Figure 1e for transect locations). Data and depth of investigation are plotted relative to LiDAR-derived land surface elevations. Piezometer locations (P1 and P2) are plotted along the B-B' transect. Oscillations in resistivity are an artifact of how data are projected onto the transect.

Information S1). The north foredune width and slope ranged from 12 to 48 m (24 ± 6.1 m) and 10-30° (18 ± 2.9°), respectively, and higher dune crests were further landward (wider foredune) and steeper (Table 1, Figures S6e, S6f, S7e, and S7f in Supporting Information S1). Dune volume and island volume varied considerably and were 36–280 and 295–929 $m^3\ m^{-1}$, respectively and correlated strongly with the described variability in the ocean-side

21699011, 2024, 4, Downloaded from https://agupubs.onlinelibrary.wiley.com/doi/10.1029/2023JF007551, Wiley Online Library on [18/06/2024]. See the Terms and Conditions (https://onlinelibrary.wiley.com/terms-and-conditions) on Wiley Online Library for rules of use; OA articles are governed by the applicable Creative Commons License

21699011, 2024, 4, Downloaded from https://agupubs.onlinelibrary.wiley.com/doi/10.1029/2023JF007551, Wiley Online Library on [18/06/2024]. See the Terms and Conditions (https://onlinelibrary.wiley.com/terms-and-conditions) on Wiley Online Library for rules of use; OA articles are governed by the applicable Creative Commons License

foredune morphology (Figure S6g in Supporting Information S1). Table 1 presents the average foredune and island volume per shoreline length contributing to the total volume along A-A'.

Although only one pre-disturbance LiDAR survey was presented, these conditions were representative as DEMs derived from this LiDAR survey were comparable to 2 years of DEMs generated from drone-based aerial imagery with photogrammetry (Dolan, 2022). Further, the morphologic characteristics of Hog Island aligned with observations from the 1970s, and more generally, with barrier islands worldwide (Armon & McCann, 1979; McCann, 1972). Unlike low-lying barrier islands, the high, established foredune on Hog Island may increase resiliency to storm impacts (Claudino-Sales et al., 2010; Houser, 2013). Variability in the foredune height, width, slope, and volume alongshore are expected to control the response (scarping and washover) to high water levels (Davidson et al., 2020; Héquette et al., 2019).

3.1.2. Fresh Groundwater Resources

Geophysical and groundwater monitoring data collected before Hurricane Fiona (August 2021–September 2022) confirmed the presence of a thin freshwater lens and demonstrated that morphodynamics and nearshore hydrodynamics impact the distribution and dynamics of fresh groundwater on Hog Island (Figure 5a). Smooth models fit raw FDEM data with an error of 17%, and models from transects repeated in each survey reliably reproduced the freshwater lens geometry. Bulk-resistivity models from coincident FDEM and TEM data (TEM1, 2, and 4 in Figure 1d and within 20 m of C-C'') collected August 2021 along the C-C'' transect aligned closely (Figure 5a), suggesting that both EM approaches were suited to freshwater lens mapping as in other small-island aquifer studies (Briggs et al., 2021; Cantelon et al., 2023).

High resistivity values at higher elevations (>0 m aMSL) were likely due to lower saturation above the water table, while high resistivities bMSL reveal a thin zone saturated with fresh water (Figure 5a). Between sea level and the transition zone top along the C-C'' transect (Figure 5a), the groundwater EC interpreted from EM resistivity data was 0.9–1.3 mS cm^{-1}, which falls within the freshwater range (Jiao & Post, 2019). The maximum freshwater lens depth (transition zone top) along this transect was 2.7 m bMSL, and from 2.7 to 6.3 m bMSL (transition zone), the groundwater EC interpreted from FDEM data increased to 30–65 mS cm^{-1}, characteristic of seawater and with no freshening from deeper aquifers (Figure 5a).

The freshwater lens geometry on Hog Island aligned with analytical solutions and field observations from other barrier islands. DGPS surveys revealed that the average water table elevation in dug pits was 0.08 m aMSL (Figures 5a and 6b). Applying the Ghyben-Herzberg relation to the average water table elevation, the bottom of the freshwater lens was estimated to be 2.9 m bMSL, comparable with the depth interpreted from the FDEM models. However, sharp-interface solutions may represent a lens that extends slightly into the transition zone. Similarly, at the C-C" transect (island dune width 130 m), the maximum freshwater lens depth (2.7 m bMSL) derived with FDEM data agreed with what was predicted by the Fetter (1972) solution (2.6 m bMSL) with the previously noted recharge and hydraulic conductivity. Accordingly, the Fetter (1972) solution was applied to pre-disturbance island widths (55–230 m, Section 3.3.1) from A-A', and the freshwater lens thickness was estimated to be 1.1–4.6 m bMSL. At the C-C'' transect (Figure 1e), the freshwater lens was limited to the dune area (i.e., recharge zone) and had an asymmetric shape weighted toward the south. Where dune topography was continuous (no blowouts), the maximum freshwater lens thickness occurred approximately in the island center (Figure 5a). Lens thickness was maintained toward the bay-side dune toe (1.7 m bMSL) but thinned toward the ocean-side dune toe (0.5 m bMSL).

Freshwater lenses less than 5 m thick are observed on similar narrow (<300 m) sand barrier islands with high aquifer recharge rates, such as Assateague Island, Maryland, USA (Masterson et al., 2014), narrow (~330 m) portions of St. George Island, Florida, USA (Schneider & Kruse, 2003), and the Outer Banks of North Carolina, USA (Bolyard et al., 1979). The high hydraulic conductivity sand that comprises Hog Island promotes fresh and saline groundwater mixing and facilitates efficient submarine groundwater discharge (SGD) that limits the freshwater lens depth and increases the transition zone thickness. A transition zone thicker than the maximum freshwater lens depth (Figure 5a) is observed on other small islands driven by tidal mixing, temporal variations in recharge (seasons or El Nino), and seawater inundation (Anderson & Lauer, 2008; Briggs et al., 2021; White & Falkland, 2010). High waves and frequent flooding occur from the north in the Gulf of St. Lawrence and drive the freshwater-seawater boundary inland closer to the dune toe, where high terrain prevents seawater flooding, and fresh precipitation recharges the aquifer. The asymmetry in the freshwater lens observed on Hog Island is

21699011, 2024, 4, Downloaded from https://agupubs.onlinelibrary.wiley.com/doi/10.1029/2023JF007551, Wiley Online Library on [18/06/2024]. See the Terms and Conditions (https://onlinelibrary.wiley.com/terms-and-conditions) on Wiley Online Library for rules of use; OA articles are governed by the applicable Creative Commons License

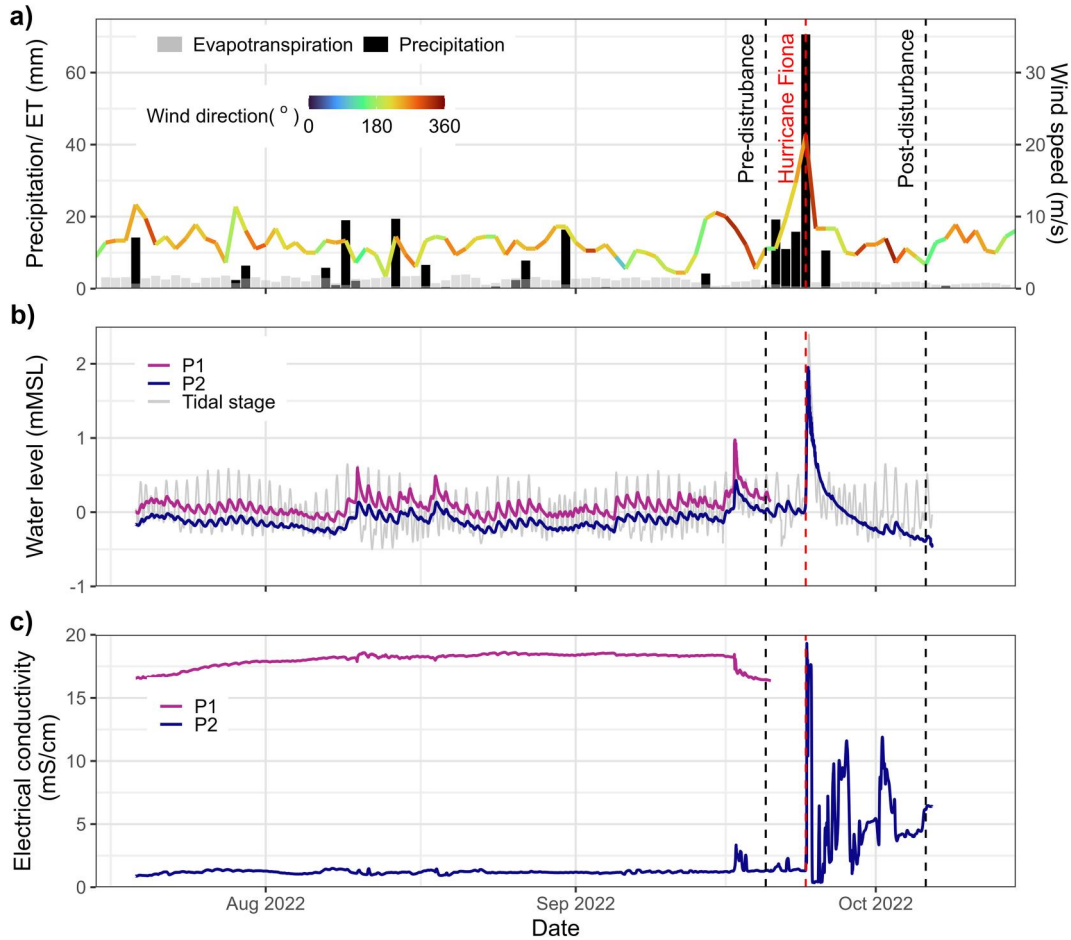

Figure 6. (a) Daily precipitation, evapotranspiration, mean wind speed, and dominant wind direction (° from North) from the climate station (ID Hog Island, 20599512, MCPEI, 2023), (b) groundwater level and surface water (gray) level at the RBR solo D wave logger, and (c) groundwater electrical conductivity observed in piezometers P1 and P2. See Figure 1e for piezometer and wave logger locations. Dashed lines indicate the dates of surveys and Hurricane Fiona, which damaged P1 and truncated the data record.

characteristic of barrier islands and may be driven by effective differences in sea level from higher wave runup on the north beach, as the north and south beach hydraulic conductivity are similar (Cartwright & Neilson, 2001; Vacher, 1988). Less dynamic water levels in the bay promote subsurface mixing between the dune toe and shoreline, forming a tube of discharging water bMSL (Figure 5a; Röper et al., 2013). These observations collectively suggest that hydrodynamic conditions in the Gulf of St. Lawrence impact the distribution of fresh groundwater, shift the hydraulic divide toward Malpeque Bay, and impact SGD. In coastal waters such as Malpeque Bay, SGD affects water quality, biogeochemical processes, ecosystems, and aquaculture operations (Seibert et al., 2021; Taniguchi et al., 2019; Wang & Du, 2016).

Pre-disturbance piezometer data show how groundwater level and EC responded to climatic and hydrodynamic forcing (Figure 6). Groundwater levels oscillated around the MSL with the dominant tidal period (Figure 6a). At P1 and P2, groundwater levels varied by 0.23 and 0.17 m, and ECs varied by 1.1 and 0.05 mS cm^{-1}, respectively, in response to the 0.87 m tidal range. Tidal signal propagation to P1 and P2 was consistent with Neilsen's (1990) conceptual model for tides in unconfined beach aquifers, and the more inland piezometer (P2) exhibited less variation in level and EC than the piezometer (P1) closer to the shoreline. Groundwater levels at P1 and P2 increased in response to precipitation (e.g., 0.6 and 0.2 m at P1 and P2, respectively on 10 August 2022); however, the largest increase in water level (0.9 and 0.5 m at P1 and P2, respectively) occurred on 16 September 2022 without precipitation or seawater flooding (no change in EC). This increase in groundwater levels was driven by a lateral propagation of pressure into the beach aquifer from high ocean levels (Figure 6b). Groundwater level and

21699011, 2024, 4, Downloaded from https://agupubs.onlinelibrary.wiley.com/doi/10.1029/2023JF007551, Wiley Online Library on [18/06/2024]. See the Terms and Conditions (https://onlinelibrary.wiley.com/terms-and-conditions) on Wiley Online Library for rules of use; OA articles are governed by the applicable Creative Commons License

EC dynamics revealed high ocean-aquifer connectivity and suggested that nearshore hydrodynamics (tides, surges, and waves) cause short-term variations in aquifer hydraulic gradients, salinity distributions, and SGD.

At the B-B' transect (coincident with piezometers, Figure 1e), the freshwater lens extended to a maximum depth of 1.1 m bMSL, and the transition zone bottom was 4.4 m bMSL (Figure 5b). On 19 September 2022, the groundwater EC in P1 and P2 was 16 and 1.3 mS cm^{-1}, respectively (Figure 6b), which closely matched the porewater EC interpreted from FDEM models at coincident depths (16 and 2.0 mS cm^{-1} at P1 and P2, respectively). At the post-disturbance dune toe location, the mean alongshore freshwater lens depth (transition zone top) was 1.7 ± 0.9 m bMSL (Figures S8a–S8c in Supporting Information S1). At C-C', dunes are high, and the transition zone top (2.6 m bMSL) and bottom (5.9 m bMSL) were deep (Figure 5c), and just southeast of this (1,250 m along A-A'), the freshwater lens was thickest (3.2 m bMSL). In contrast, no freshwater lens was observed at the narrowest island widths where dune crests are low (1,100–1,150 m; Figures S8a–S8c in Supporting Information S1). The average depth of the transition zone bottom was 5.3 ± 1.1 m bMSL, and patterns alongshore follow the variation in the transition zone top (max depth 7.7 m bMSL at high dunes). However, the transition zone thickness had less alongshore variability (3.2 ± 0.6 m) than the freshwater lens thickness. The volume of fresh groundwater in the beach aquifer (post-disturbance shoreline to dune toe) varied considerably from 0 to 10.5 $m^3\ m^{-1}$ (3.8 ± 3.1 $m^3\ m^{-1}$) alongshore, and more fresh groundwater occurred under high dune crests (Figures S8a and S8e in Supporting Information S1). The brackish groundwater volume ranged from 5.5 to 23.8 $m^3\ m^{-1}$ (14.2 ± 3.2 $m^3\ m^{-1}$) alongshore, and where no freshwater lens was observed (narrow widths and low dunes), brackish water volumes were highest (Figures S8a, S8b, S8f in Supporting Information S1). Results demonstrate that local-scale topographic features controlled the freshwater lens and transition zone morphology, local groundwater flow patterns, and salt transport as in other coastal aquifer studies (Paldor, Stark, et al., 2022; Zhang et al., 2016).

3.2. Disturbances Following Hurricane Fiona

3.2.1. Disturbed Island Morphology

Satellite imagery collected the day after the storm (25 September 2022) revealed suspended sediment plumes that extended up to 1,100 m offshore (Figure 3b). Drone-based imagery collected 11 days after the storm revealed scarping and widespread foredune erosion, but no new washover fans or dune blowouts (Figures 3d, 3f, and 4a, Figure S4b in Supporting Information S1). The post-disturbance beach was void of vegetation and debris, and apart from a small amount of sand deposited along the shoreline and dune scarp base, there was no evidence that eroded material was redistributed to the beach (Figures 3d, 3f, and 4a). Together, satellite and drone imagery, climate, wave, and groundwater monitoring data (Sections 2.2 and 3.2.2) suggest that seawater inundated the beach, infiltrated and destabilized sediment, and caused slope failure, while wave attack undercut at the foredune base and caused mass failure via collapse.

A comparison of pre- and post-disturbance surveys revealed north foredune erosion that increased the beach width by 55% and alongshore beach volume by 127% (Table 1, Figures 4a, and 4c, Figures S6a–S6c in Supporting Information S1). Continuous scarping of the foredune was observed along the A-A' transect (Figure 3f), and characteristic of scarping, the dune slope increased by 22% (Table 1). Along most of the alongshore A-A' transect, the dune scarp reached the dune crest, and the maximum scarp height at the highest dune crest was 14.9 m (Figures S6d and S6e in Supporting Information S1). Erosion caused the north dune crest to move landward by 5.2 ± 4.4 m on average, and dune crest elevations changed by −2.9 to +3.8 m (0.7 ± 0.6 m; Figures 4a and 4c, Figures S6e and S7e in Supporting Information S1). Less lateral erosion occurred in the northwest (350–850 m), and the greatest occurred in the southeast (1,250–1,750 m) of the A-A' transect (Figures 4a and 4c). There was no significant relationship between lateral dune erosion and pre-disturbance dune height or beach width (Figure 7a).

Dune scarping reinforced alongshore patterns; for example, the height of low-elevation dune crests decreased more than that of high-elevation dune crests (Figure S6e in Supporting Information S1). This suggests that erosion impacts were controlled by alongshore patterns in the water levels and wave energies that acted on the dune (Davidson et al., 2020; Houser et al., 2008). Scarp heights on Hog Island were higher than those observed following similar magnitude high water levels in the Gulf of St. Lawrence that impacted barrier islands in PEI (George et al., 2021). The high scarp was perhaps predictable given the high dune heights and narrow pre-disturbance beach widths that increased the likelihood of high-water levels reaching the dune. Erosion may degrade habitats for island species; however, dune scarps create opportunities for early successional species

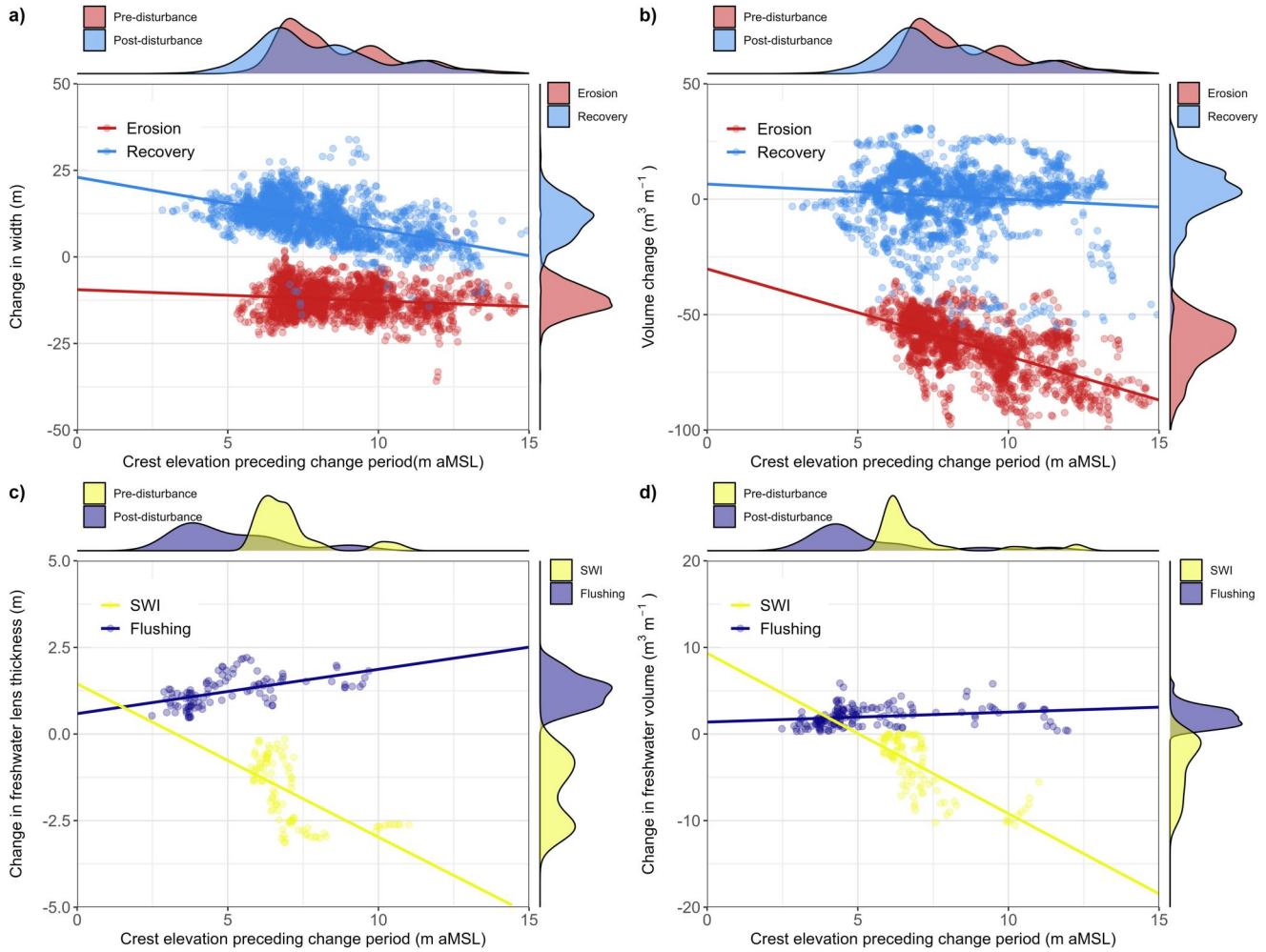

Figure 7. Joint probability plots of morphologic evolution and groundwater resource changes. Top panels show the relationship between ocean-side dune crest elevation and the change in (a) dune width and (b) island volume over the erosion and recovery periods. Bottom panels show the relationship between ocean-side dune crest elevation and the change in (c) freshwater lens thickness and (d) freshwater volume between SWI and flushing periods. In all panels, the top histograms correspond to the dune crest elevation preceding the change period, and the right histograms correspond to the change over the erosion/SWI (post-disturbance minus pre-disturbance) and recovery/flushing (recovery minus post-disturbance) periods.

(Liebowitz et al., 2016). Following Hurricane Fiona, the wide flat beach (no change in beach slope from pre-disturbance) may help dissipate wave energy during future storm events and contribute to recovery (Davidson et al., 2020). However, a high scarp is associated with dune instability as it can increase vulnerability to dune crest collapse and blowouts under future high water levels (Houser, 2013). This, paired with the large volume of accretion required to replace eroded sediment, is expected to prolong recovery times (Hesp, 1988).

During Hurricane Fiona, a large volume of sediment was lost from the subaerial beach-dune system (all metrics presented in Table 1). For example, the average dune and island volume per meter of shoreline decreased by 55% and 12%, respectively (Figures 4a and 4c). After erosion, the foredune volume varied from 7 to 110 $m^3\ m^{-1}$ (Figures S6g and S7g in Supporting Information S1), and more sediment was lost from the highest dune crests in the southeast (Figures 4a, 4d and 7b). A small amount of accretion occurred on the bay side, and the south dune volume increased by 11 $m^3\ m^{-1}$ on average (Figure 4a, Figures S6n and S7n in Supporting Information S1). There was no evidence of washover, and thus, backslope accretion was likely driven by aeolian sediment transport. In total, Hurricane Fiona eroded 12% of the monitoring area volume (Table 1); however, if sediment was redistributed to the nearshore and offshore zones, it may be returned in the future (Figures 3b, Houser et al., 2008; Marmoush & Mulligan, 2020).

21699011, 2024, 4, Downloaded from https://agupubs.onlinelibrary.wiley.com/doi/10.1029/2023JF007551, Wiley Online Library on [18/06/2024]. See the Terms and Conditions (https://onlinelibrary.wiley.com/terms-and-conditions) on Wiley Online Library for rules of use; OA articles are governed by the applicable Creative Commons License

21699011, 2024, 4, Downloaded from https://agupubs.onlinelibrary.wiley.com/doi/10.1029/2023JF007551, Wiley Online Library on [18/06/2024]. See the Terms and Conditions (https://onlinelibrary.wiley.com/terms-and-conditions) on Wiley Online Library for rules of use; OA articles are governed by the applicable Creative Commons License

Volumetric sediment loss along the A-A' monitoring transect was high relative to losses observed on barrier islands impacted by hurricanes, as summarized in Table 4 of Sherwood et al. (2023). The volume of sediment lost was larger than all tabulated events except for the impact of Hurricane Sandy (Sopkin et al., 2014). Sediment loss was comparable to that observed at North Core Banks, North Carolina, where Hurricane Dorian caused sound-side washouts and offshore sediment transport (Sherwood et al., 2023), and Santa Rosa Island, Florida, following three hurricanes that impacted the island between 2004 and 2006 (Houser & Hamilton, 2009). The high foredune on Hog Island prevented overwash; however, because sediment was not redistributed to washover deposits, a large volume of sediment was lost. As such, the volumetric loss of sediment following this event was similar to outwash on low-elevation islands (Hapke et al., 2013; Houser et al., 2008; Priestas & Fagherazzi, 2010). The transport of sediment and associated nutrients to the nearshore will contribute to the formation and function of nearshore ecosystems (Liebowitz et al., 2016).

3.2.2. Groundwater Salinization

Piezometer data revealed SWI impacts and early recovery, but the data record was limited. Antecedent beach groundwater levels were low, resulting in a high vertical hydraulic gradient between floodwaters (pluvial and seawater) and the beach water table that drove rapid infiltration (Cardenas et al., 2015). Groundwater levels rose 1 m (with no change in EC) in response to rainfall on 23 September 2022 that preceded the arrival of peak storm surge and high waves that flooded the beach and increased the groundwater level by an additional 1 m and EC by 19 mS cm^{-1} (Figures 2e and 6). Before the storm, land surface elevations at P1 and P2 were 0.9 and 1.5 m aMSL, respectively, so the 2 m increase in groundwater level would have completely saturated the beach (Figure 6a). The groundwater EC in P2 only increased to 20 mS cm^{-1} and did not reach the EC of ocean water (>35 mS cm^{-1}), suggesting that as seawater infiltrated, it was diluted by freshwater (Figure 6c).

Antecedent conditions on Hog Island had the potential to exacerbate SWI impacts. An influx of seawater on Hog Island altered the groundwater flow field, and density differences initially drove the spread of infiltrated seawater (Post & Houben, 2017). However, high precipitation rates during the storm recharged the aquifer, decreased aquifer salinity, and ultimately moderated SWI impacts, similar to the observations of Terry and Falkland (2010) and Vithanage et al. (2012). This result indicates that fresh recharge preceding and during seawater flooding may expedite aquifer recovery in addition to recharge after flooding (e.g., Gingerich et al., 2017). On PEI, extreme precipitation during hurricanes can rapidly recharge aquifers and drive high rates of SGD (Pavlovskii et al., 2023). During the storm, 0.5–1 m of vertical erosion occurred along much of the beach (Figure 4a). Following the observations of Cardenas et al. (2015) and in accordance with the conceptual model of Cantelon et al. (2022), vertical erosion during this event decreased the vadose zone thickness, limited seawater recharge, and decreased the volume of infiltrated seawater (Liu & Tokunaga, 2019). However, time-series data of vertical erosion and infiltration fluxes are required to better disentangle these processes. Swash zone beach-aquifer interactions are recognized as an important factor contributing to sediment movement on beach faces (Cartwright et al., 2006). High vertical seepage at intermediate elevations, coastal berms, and scarps can contribute to sediment mobilization and influence morphology. Thus, patterns in groundwater levels during this storm event likely contributed to geotechnical risks such as liquefaction and failure (Paldor, Stark, et al., 2022).

Once floodwaters receded, groundwater levels returned to the pre-storm level in 1 week, which demonstrates the strong influence of the mean sea level elevation on island groundwater levels (Figure 6b). In highly permeable sands, the water table is close to the MSL, and thus, 0.5–1.0 m of vertical beach erosion decreased the vadose zone thickness after the water table returned to typical levels. The groundwater EC in P2 showed evidence of flushing in the days after the storm (<11 days), but EC was highly variable and increased in response to coastal hydrodynamics (e.g., spring tide 2 October 2022) (Figure 6b). FDEM data collected 11 days after the storm revealed that the EC of beach groundwater below MSL ranged from 9.5 to 37.7 mS cm^{-1} (Figures 5d and 5e). No fresh groundwater was observed in the post-disturbance survey area, making the freshwater lens 0 m thick. On average, 12.5 ± 3.1 m^3 m^{-1} of freshwater loss occurred alongshore, and more SWI occurred at high dune crests (Figure 7d, Figures S8a–S8e in Supporting Information S1). The decrease in the cross-shore freshwater lens width was predicted by foredune erosion alongshore (Section 3.2.1; Figures 5d and 5e).

Beach aquifer salinization was consistent alongshore, and the flat beach prevented seawater ponding and localized zones with exacerbated SWI (Cantelon et al., 2023; Terry & Falkland, 2010). Previous studies have found that low beach elevations experience more extensive coastal flooding and concomitant vertical SWI

following a storm (Holding & Allen, 2015a; Nordio et al., 2023). Results from this study further demonstrate that lateral erosion can cause vertical SWI to extend an equivalent cross-shore distance from the shoreline at both low and high coastline elevations (preceding erosion) and cause more freshwater loss at higher elevations (Figure 7d).

FDEM models had high resistivities aMSL due to desaturation from groundwater level recession in the days following the storm (Figures 5d, 5e, and 6b). A thin zone of brackish water (EC between 7.9 and 9.5 mS cm^{-1}) occurred between sea level and 1.6–3.5 m bMSL (Figures 5d and 5e) after the storm. Beach aquifer stratification was maintained through time by the density difference between less dense brackish water that overlaid denser saline water (Figures 5d and 5e; Post & Houben, 2017). At the post-disturbance dune toe, the average depth of the transition zone bottom was 2.3 ± 0.5 m bMSL, and under high dunes the transition zone was thicker (Figure S8d in Supporting Information S1). Pre-and post-disturbance FDEM data along the B-B' and C-C' transects (Figure 1e) revealed no fresh or brackish water within 25 m of the shoreline, indicating that the tides and waves limit fresh aquifer development along the shoreline. Between 25 and 45 m from the shoreline, where beach elevations are higher and dunes are proximal, the transition zone depth increased with distance from shore (Figures 4d and 4e). Alongshore, there was 8.2–17.8 m^3 m^{-1} of brackish groundwater (11.8 ± 2.1 m^3 m^{-1}; Figure S8f in Supporting Information S1). Brackish water from mixing with infiltrated precipitation and background fresh groundwater flow is the first sign of beach aquifer recovery (Figures 5d and 5e). Higher and wider island locations had larger volumes of brackish groundwater (Figures S8a, S8b, and S8f in Supporting Information S1) because there was a greater volume of fresh groundwater in the island interior that flushed the beach aquifer as it discharged toward the coast. This aligned with previous work that found that land-sea hydraulic gradients dominate initial recovery in the absence of post-storm fresh recharge (Holding & Allen, 2015a; Post & Houben, 2017).

3.3. Signs of Recovery Nine Months After the Storm

3.3.1. Recovering Island Morphology

In May 2023, 9 months after the storm, signs of morphologic recovery were evident in the derived orthomosaic image (Figure S4c in Supporting Information S1). The dune scarp was still visible, but accretion was apparent along the berm and the dune scarp base. No vegetation recolonized the beach or dune slope, but this was likely due to the colder months between surveys. Table 1 shows that the beach recovered to the pre-disturbance width, and the beach volume decreased relative to pre- and post-disturbance surveys, as beach elevations decreased and sediment was transported into the beach-dune transition zone (Figures 4b and 4c). Along much of the A-A' transect, accretion along the dune scarp formed a new dune ramp shifted toward the shoreline and restored the foredune slope and total island dune width to within 2% of pre-disturbance (Table 1, Figures 4b and 4c). Alongshore, the change in foredune width varied, and some locations increased by up to 34 m (<100 m alongshore) while others decreased by up to 4 m (1,250 m alongshore) (Figure 4d). Accretion was insufficient to rebuild the foredune to the pre-disturbance height (Figure 4d). North foredune volume generally increased (Table 1) and the maximum increase was 190 m^3 m^{-1} (1,350 m alongshore), while other locations decreased by up to 50 m^3 m^{-1} (650–950 m alongshore). Table 1 highlights that the total volume of the monitoring area only increased by 1% from post-disturbance (89% of pre-disturbance), which was lower than the average increase in the ocean-side foredune volume because of backslope erosion (Figures 4b, 4d, and 7b). Little morphologic recovery occurred by May 2023 and the beach-dune system was still in a transitional stage.

During moderate winter storms, alongshore locations with wider beaches better dissipated wave energy and had more foredune accretion (Table 1, Figures 4b–4d). The percent recovery (to pre-disturbance) of high dunes was less than that of lower dunes as a greater volume of sediment is required to rebuild the high foredune completely, and high scarps are prone to instability from higher wind velocity speedup (Hesp & Smyth, 2016). While wider island locations with low dune heights had accretion (0–250 m alongshore), lower dunes at narrower island locations eroded further (650–950 m alongshore, Figure 7b). Houser et al. (2015) attributed slow recovery on narrow, low-lying barrier islands to sediment availability. Thus, the recovery patterns alongshore may reflect (a) sediment supply tied to alongshore sediment transport to the southeast (Armon & McCann, 1977) and (b) that lower dune heights are more prone to erosion and sediment redistribution from northern winter winds and high-water levels. Collectively, these results suggest that erosion and recovery processes reinforce alongshore morphology patterns (i.e., low dune heights and narrow widths) as they are spatially coupled to the pre-disturbance beach and dune morphology (Davidson et al., 2020; Houser, 2013).

21699011, 2024, 4, Downloaded from https://agupubs.onlinelibrary.wiley.com/doi/10.1029/2023JF007551, Wiley Online Library on [18/06/2024]. See the Terms and Conditions (https://onlinelibrary.wiley.com/terms-and-conditions) on Wiley Online Library for rules of use; OA articles are governed by the applicable Creative Commons License

21699011, 2024, 4, Downloaded from https://agupubs.onlinelibrary.wiley.com/doi/10.1029/2023JF007551, Wiley Online Library on [18/06/2024]. See the Terms and Conditions (https://onlinelibrary.wiley.com/terms-and-conditions) on Wiley Online Library for rules of use; OA articles are governed by the applicable Creative Commons License

Morphologic recovery following erosion is typically driven by landward sediment transport from the swash and nearshore zones (Héquette et al., 2019; Houser, 2013). Limited recovery on Hog Island suggests that sediments redistributed to nearshore and offshore zones have not returned to the island, which may be because high winter waves frequently reworked the nearshore and low-elevation beaches (Figure S3a in Supporting Information S1), and winter ice cover limited landward sediment transport (Houser & Hamilton, 2009). Recovery rates on other barrier islands vary depending on whether the island was scarped or overwashed, and observations from Hog Island are consistent with scarping or bay-side outwash that drives offshore sediment transport (Hesp, 2002; Houser & Hamilton, 2009). Therefore, the recovery observed 9 months after Hurricane Fiona was likely from reworked beach sediments (Figure 4b). After similar-magnitude events, full morphologic recovery takes up to a decade and is slower at high elevations (Houser & Hamilton, 2009).

The high dune scarps are still present and pose an ongoing geotechnical hazard that decreases recreational use, aesthetic value, and habitats for sensitive species, as few early successional species have established along the scarp (e.g., Klein et al., 2004; Schlacher et al., 2008). The future recovery of Hog Island will require a long return period between high water levels that can reach the recovery dune toe (wave run-up of 1.2 m aMSL), which would occur at significant wave heights over 3.7 m with a return period of 1.25 years based on analysis of hindcasted wave data (Figure S2 in Supporting Information S1; Nielsen & Hanslow, 1991). The morphology of Hog Island pre-disturbance was consistent with observations from over 50 years ago despite many high wave events (11 events with 4.5 m significant wave heights between 1954 and 2018). Further, high dune elevations on Hog Island suggest an available nearshore sediment supply, which may support island recovery in the present wave climate. Thus, the potential for Hog Island to recover the remaining 1.3×10^5 m^3 of lost sediment depends on how far offshore it was transported. Without an influx of sediment from a nearshore, alongshore, or offshore source, Hog Island may trend towards a new "lower and narrower" equilibrium state.

3.3.2. Groundwater Flushing

FDEM surveys and pits dug 9 months after Hurricane Fiona were used to assess beach aquifer flushing and recovery (Figures 5f and 5g). The B-B' and C-C' transects (Figure 1e) showed a zone of low-EC groundwater under the north dune that suggested moderate recovery of the beach aquifer (Figures 5f and 5g). Within 35 m of the north shoreline, beach groundwater EC ranged from 25 to 61 mS cm^{-1} (Figures 5d and 5e). The water table in dug pits was within 10 cm of MSL and had an EC of 35 and 26 mS cm^{-1} at the location of P1 and P2, respectively, which aligned with the porewater EC interpreted from FDEM models at coincident locations (38 and 27 mS cm^{-1} at P1 and P2, respectively; Figure 5f). The freshwater lens (transition zone top) extended to an average depth of 1.3 ± 0.5 m bMSL at the location of the post-disturbance dune toe but varied from 0.5 to 2.4 m bMSL deep alongshore. The fresh (0.4–1.6 mS cm^{-1}) beach groundwater volume (post-disturbance dune toe to the north shoreline) ranged from 0.3 to 4.9 m^3 m^{-1}. The transition zone bottom was between 3.7 and 6.7 m bMSL (5.3 ± 0.7 m bMSL) and was thicker (4.0 ± 0.4 m) than in pre- and post-disturbance surveys. The brackish groundwater volume ranged from 30 to 86 m^3 m^{-1}. Full recovery to pre-disturbance conditions was not observed as the lens in the recovery survey was thinner (1.3 ± 0.4 m bMSL) than the pre-disturbance survey (1.7 ± 0.9 m bMSL) and shifted landward. Further, the total volume of fresh beach groundwater in the FDEM survey (201 m^3) was only 48% of the pre-disturbance volume (392 m^3) (Figures 5f, 5g, and 7d, Figures S8c and S8e in Supporting Information S1). Foredune accretion controlled the cross-shore position of the freshwater lens and the transition zone thickness (Figure 5), but foredune height better predicted recovery as higher dune crests had a thicker freshwater lens and a greater fresh groundwater volume (Figures 5f, 5g, 7c, and 7d).

The major limitation of this work was that only one survey 9 months after the storm was used to assess recovery. Thus, the impact of individual recharge or high-water level events (e.g., winter nor'easter storms) on recovery could not be evaluated. Flushing observed in the recovery FDEM survey (Figures 5f and 5g) can be explained by fresh recharge through the winter and spring and high horizontal hydraulic gradients that drive fresh groundwater flow from the dunes to the ocean. Figure S1 in Supporting Information S1 shows that over the winter months (November-February), many precipitation events would have contributed to fresh recharge that flushed the beach. Although winter recharge would have contributed to aquifer flushing, high wind speeds, particularly from the north (Figure S1 in Supporting Information S1), bring higher winter wave heights in the Gulf of St. Lawrence (Figure S3 in Supporting Information S1). As such, flushing through the winter months was likely limited by high waves that flooded the beach between December and February (Figures S1 and S3 in Supporting Information S1). Greater flushing likely occurred in the spring (March-May) when precipitation was more

21699011, 2024, 4, Downloaded from https://agupubs.onlinelibrary.wiley.com/doi/10.1029/2023JF007551, Wiley Online Library on [18/06/2024]. See the Terms and Conditions (https://onlinelibrary.wiley.com/terms-and-conditions) on Wiley Online Library for rules of use; OA articles are governed by the applicable Creative Commons License

moderate, but lower wind speeds and wave heights decreased beach flooding (Figures S1 and S3 in Supporting Information S1). Results demonstrate that aquifer recovery was tied to foredune accretion, as dunes proximal to the coast limit beach flooding and protect the island area receiving fresh recharge. Previous work found that low-elevation and high-permeability aquifers were more susceptible to salinization but flushed faster (Anderson & Lauer, 2008; Holding & Allen, 2015b; Yang et al., 2015). Recovery on Hog Island was delayed from what might have been expected based on its hydrogeological characteristics, and paired monitoring data indicate that this delay may have been driven by rapid foredune erosion and increased flooding during winter nor'easters. Hydrodynamics and morphodynamics will continue to control aquifer recovery in the future.

3.4. Implications for Understanding and Monitoring Coastal Processes in a Changing Climate

The results of this study go beyond previous studies that considered the impacts of either erosion or SWI from storm surge in isolation and help fill the gap in understanding how rapid foredune erosion impacts freshwater resources. Coastal topography controls the extent of inundation, wave/surge runup, and flooding recession, and the results further demonstrate that feedbacks between surface hydrodynamics and morphodynamics control aquifer salinization and flushing. Paired monitoring data show that erosion and dune topography are the dominant drivers of SWI and flushing on Hog Island. While past work considered lateral SWI from perturbations in groundwater hydraulic heads and sea levels (Werner et al., 2013) and vertical SWI from decadal erosion and flooding (Cantelon et al., 2023; Stanic et al., 2024), the present study demonstrates that coastal erosion can cause rapid vertical and lateral SWI over short timescales (<1 year) that persists if morphologic recovery does not occur. Islands come in many shapes and geologies, and the results of this study apply to relatively unfortified, low-lying islands with erodible sediments, particularly small island developing states, that often have insufficient resources to build extensive coastal defense structures (Nunn et al., 2021; Pelling & Uitto, 2011). Results indicate that even moderate erosion rates can cause seawater to encroach landward in the surface and subsurface, degrading natural resources and transforming ecosystems. These findings have global implications as a quarter of sandy coastlines are eroding at over 0.5 m year^{-1} (Luijendijk et al., 2018). Although these results are not directly applicable to anthropogenically hardened coastlines and heavily urbanized hydrologic regimes, they are relevant to rural and urban populations that rely on groundwater wells located in more natural land use types (away from urban zones) that may be similar to this study site.

Along sandy coastlines, both surface and subsurface impacts must be considered to comprehensively understand geotechnical and SWI hazards following storms and cascading effects on ecosystems and coastal populations. Varied topographic and hydrological regimes on coastal dunes increase ecological niches that support diverse ecosystems (Everard et al., 2010); however, erosion and SWI can selectively kill salt-intolerant species, transform ecosystem functioning (Guimond & Michael, 2021), and reduce ecological services (Paprotny et al., 2021). Sediment-ocean and atmosphere-ocean interactions play an essential role in marine ecosystems and contribute to biological productivity (e.g., Santos et al., 2021). Sediment loading from erosion and high saline SGD rates following storms may impact contaminant fate and transport (e.g., Threndyle et al., 2022; Wong et al., 2015). Such processes can impact nearshore water quality and disturb biogeochemical processes, ecosystems, and aquaculture operations (Chambers et al., 2013; Rakhimbekova et al., 2023). Results from this unpopulated island suggest that coastal populations along unfortified, sandy coastlines may expect geotechnical hazards (e.g., Paldor, Stark, et al., 2022), infrastructure damage (e.g., Habel et al., 2020; Parkinson, 2021), agricultural losses (e.g., Guimond & Michael, 2021; LeRoux et al., 2023; Tackley et al., 2023), groundwater-driven surface flooding (e.g., Housego et al., 2021), and compromised drinking water supplies (Michael et al., 2017). There is a need to understand how these processes along natural coastlines compare with those along developed coasts, where hardened structures may reduce flooding but consequently slow aquifer recovery (Lee et al., 2019). Future studies should also consider how erosion and SWI can interact with groundwater pumping and urbanized hydrologic regimes (Stanic et al., 2024).

To better understand erosion/accretion and SWI/flushing dynamics, future monitoring must span disciplines and collect spatiotemporally distributed surface and subsurface data (Cantelon et al., 2022; Houser et al., 2015). Large storm events can drive rapid impacts to barrier islands, while dune and aquifer recovery can take years or may never occur due to ever-changing marine, climatic, and anthropogenic influences (Davidson et al., 2020; Paldor, Frederiks, & Michael, 2022). The disparate timescales of storm impacts and recovery are challenging to monitor as they require rapid and frequent deployments that are costly and prone to failure as instruments are frequently

21699011, 2024, 4, Downloaded from https://agupubs.onlinelibrary.wiley.com/doi/10.1029/2023JF007551, Wiley Online Library on [18/06/2024]. See the Terms and Conditions (https://onlinelibrary.wiley.com/terms-and-conditions) on Wiley Online Library for rules of use; OA articles are governed by the applicable Creative Commons License

lost or damaged. This contributes to a scarcity of spatiotemporally distributed field data that capture pre-storm conditions, post-storm impacts, and complete morphologic and aquifer recovery. Topographic survey methods (LiDAR and aerial imagery) allow for short-term, high-resolution, and quantitative assessments of morphologic change and can serve as a basis for predicting SWI impacts. However, short-term coastal monitoring only represents a snapshot of time, and individual storm impacts must be evaluated in the context of present, recent, and long-term observations of island morphology and groundwater salinity as well as hydrodynamic and climatic drivers (Masselink et al., 2016). Alongshore variations in pre-storm conditions (morphology, groundwater salinity, hydrodynamics) control erosion/SWI and recovery in a repeatable pattern that reinforces trends (Cantelon et al., 2023; Houser, 2013). This suggests that historical patterns of morphologic evolution (transgressions and washover) derived from satellite or aerial imagery should be the foundation of vulnerability assessments considering future SWI susceptibility.

While the proliferation of LiDAR technology will advance monitoring, there is a need for low-cost instruments capable of capturing spatially distributed groundwater conditions. Tracers such as heat may be one approach for collecting dense networks of time-series data on vertical erosion and seawater infiltration during storms (Cantelon & Kurylyk, 2023). In addition to monitoring, numerical modeling of future hydrodynamic conditions, morphodynamics, and groundwater response is required, and the results of this study show there is an increasing need for coupled surface-subsurface models capable of simulating these dynamics. Future work should expand the capabilities of coupled surface-subsurface models (e.g., Hydrogeosphere, Brunner & Simmons, 2012) to model morphodynamics, and coupled morphodynamic-hydrodynamic models to simulate groundwater dynamics (e.g., XBEACH, Roelvink et al., 2010).

Results show prolonged impacts from a rapid flooding event (>9 months). For barrier islands in the North Atlantic, flooding, erosion, and associated SWI will be an important vulnerability consideration and challenge for management (Housego et al., 2021), given high rates of sea-level rise and more intense storms tracking further north (Garner, 2023). Further, along unfortified sandy coastlines, gradual and rapid changes in coastal morphology—that are likely to increase with sea-level rise—will control the volume of freshwater resources (Holt et al., 2019; Huizer et al., 2017). Higher sea levels (surges and SLR) will cause more frequent coastal flooding and erosion that will in turn increase vertical SWI and have long-term impacts on potable freshwater resources. For islands with limited adaptive capacity, the loss of land and freshwater resources will increase reliance on expensive and energy-intensive alternatives or force emigration (Storlazzi et al., 2018). Shorter return times between high water level events may limit morphologic and aquifer recovery and prolong risks to coastal populations (Vousdoukas et al., 2020). A strong connection between island morphology and groundwater resources observed over short time scales (single event) suggests that there will be a long-term co-evolution in the future. Along these lines, while washover, inlet formation, and aeolian transport may cause erosion and SWI on the ocean-side in the short term, associated sediment transport to the bay side may maintain island width and drive a co-migration of the island and freshwater lens landward that, in the long-term, keeps pace with rising sea levels (Wolinsky & Murray, 2009). Flushing and aquifer recovery are driven by fresh recharge in areas protected by dune topography. Thus, the recovery of barrier island aquifers to extreme events in the future may also be accelerated or prolonged depending on how local recharge regimes increase (wetter climate) or decrease (drier climate) as the climate changes (Richardson et al., 2024). Achieving long-term coastal resilience in an era of rapid global change requires innovative land and water management strategies based on a thorough understanding of the interrelated drivers and impacts of coastal flooding, erosion, and aquifer salinization (McDonald et al., 2019).

4. Conclusion

Storm surges during coastal storms, such as hurricanes, are known to cause rapid flooding, erosion, and SWI; however, the related impacts on surface and subsurface domains are often assessed in isolation by separate disciplines. This study analyzed paired morphologic and hydrogeologic monitoring data from pre-disturbance, post-disturbance, and recovery periods on a sandy-barrier island impacted by Hurricane Fiona in 2022. Detailed field data collected on Hog Island, PEI, using drone-based LiDAR and electromagnetic geophysics, is among the first to show the connection between rapid dune erosion and SWI on a barrier island impacted by a hurricane. The results demonstrated that island morphodynamics control aquifer salinization and flushing. Alongshore variations in dune height and width controlled the distribution of groundwater before disturbance. During Hurricane Fiona, the ocean-side Hog Island foredune experienced, on average, 12 m of lateral erosion that strongly controlled the

21699011, 2024, 4, Downloaded from https://agupubs.onlinelibrary.wiley.com/doi/10.1029/2023JF007551, Wiley Online Library on [18/06/2024]. See the Terms and Conditions (https://onlinelibrary.wiley.com/terms-and-conditions) on Wiley Online Library for rules of use; OA articles are governed by the applicable Creative Commons License

extent of land surface inundation and the volume of groundwater salinization. Slow morphologic recovery facilitated more coastal flooding and delayed groundwater flushing relative to what would have been expected for the site if no erosion occurred. Coastlines that experience significant coastal erosion during storms and slow morphologic recovery will be more vulnerable to salinization, lose a greater volume of potable freshwater, and have longer aquifer recovery. Results revealed repeatable patterns between impacts (erosion and SWI) and recovery (accretion and flushing) that reinforce pre-existing trends in island and freshwater lens morphology; thus, the effects of individual storms should be evaluated in the context of long-term morphologic, hydrodynamic, and groundwater monitoring data.

This study represents an initial step toward understanding the connection between hydro-, morpho-, and groundwater dynamics caused by ocean surges. Monitoring on this unpopulated island reveals that erosion may punctuate freshwater decline in an era of intensifying ocean storms, a finding of relevance to sandy coastlines facing high erosion rates worldwide. Results highlight that coastal topography and morphologic changes can serve as a SWI vulnerability indicator, as topography determines spatiotemporal patterns of seawater infiltration and aquifer recharge, and thus SWI and flushing. Collectively, the data highlight the importance of considering morphology in freshwater vulnerability assessments, adaptation planning, and coastal land and water resource management decisions. Likewise, the results show the importance of considering fresh groundwater loss when quantifying the ecological and economic impacts of coastal erosion. Future work should monitor and model these related processes to understand how these threats transfer to other coastal zones. The processes presented in this study are timely in an age of rising seas and intensifying coastal storms as the return period between extreme water levels that cause flooding will decrease, transform coastal morphology, and drive long-term SWI along low-lying portions of the global coastline.

Data Availability Statement

All the morphologic and hydrogeologic data needed to evaluate the results presented in this paper are archived on Borealis (https://borealisdata.ca/dataset.xhtml?persistentId=doi:10.5683/SP3/KE5YRM). For each data type, a "read me" file explains the files. Meteorological data for Hog Island were provided by Jardine, D.E. for MCPEI at https://www.hobolink.com/p/eff9c129a08a05574e2e25dd74d4ec41. Hindcast wave data and historical wave data are available from Fisheries and Oceans Canada (DFO) by request at https://www.meds-sdmm.dfo-mpo.gc.ca/isdm-gdsi/waves-vagues/index-eng.htm. Planet satellite imagery is available by request from https://api.planet.com.

Acknowledgments
We wish to extend special thanks to the Lennox Island First Nation for access to their land. In addition, we would like to thank Blake Bernard and the Lennox Island Guardians for their support with logistics, boat transport, and fieldwork. Thank you to the PEI Watershed Alliance and the Mi'kmaq Confederacy of PEI for their generosity with funding and in-kind support. Greg Baker (St. Mary's University) and Antoin O'Sullivan (University of New Brunswick) provided helpful technical assistance with LiDAR data processing. Further, this research was supported by the Canada Research Chairs Program and a MEOPAR Early Career Award, MEOPAR Knowledge Mobilization Grant, and NSERC Discovery Grant (RGPIN-2018-05420) awarded to B. Kurylyk and an American Geophysical Union Horton Research Grant awarded to J. Cantelon. J. Cantelon was also supported by scholarships from NSERC, the Killam Trust, the NSGS program, the Canadian Water Resources Association (Dillon Scholarship), and the Canadian Geophysical Union (Don Gray Scholarship). The manuscript for this study was reviewed and approved by the L'nuey/Mi'kmaq Confederacy of PEI Research Ethics Board. We thank the Associate Editor and three anonymous reviewers who considered our work and provided feedback to improve the quality of our work.

References

Aarhus Geosoftware. (2023). Aarhus Workbench ground conductivity module 6.7.1 [Software]. *Aarhus Geosoftware*. Retrieved from https://www.aarhusgeosoftware.dk/download-aarhus-spia

Allen, R. G., Pereira, L. S., Raes, D., & Smith, M. (1998). *Crop evapotranspiration: Guidelines for computing crop water requirements (No. 56)*. FAO Irrigation and Drainage.

Anderson, W. P. (2002). Aquifer salinization from storm overwash. *Journal of Coastal Research*, *18*(3), 413–420. Retrieved from https://www.jstor.org/stable/4299090

Anderson, W. P., & Lauer, R. M. (2008). The role of overwash in the evolution of mixing zone morphology within barrier islands. *Hydrogeology Journal*, *16*(8), 1483–1495. https://doi.org/10.1007/s10040-008-0340-z

Archie, G. E. (1942). The electrical resistivity log as an aid in determining some reservoir characteristics. *Transactions of the AIME*, *146*(01), 54–62. https://doi.org/10.2118/942054-G

Armon, J. W. (1980). Changeability in small flood tidal deltas and its effects, Malpeque barrier system, Prince Edward Island. In *The Coastline of Canada: Littoral processes and shore morphology* (pp. 41–50). Geologic Survey of Canada.

Armon, J. W., & McCann, S. B. (1977). Longshore sediment transport and a sediment for the Malpeque barrier system, southern Gulf of St. Lawrence. *Canadian Journal of Earth Sciences*, *14*(11), 2429–2439. https://doi.org/10.1139/e77-211

Armon, J. W., & McCann, S. B. (1979). Morphology and landward sediment transfer in a transgressive barrier island system, southern Gulf of St. Lawrence, Canada. *Marine Geology*, *31*(3–4), 333–344. https://doi.org/10.1016/0025-3227(79)90041-0

Ataie-Ashtiani, B., Volker, R. E., & Lockington, D. A. (1999). Tidal effects on sea water intrusion in unconfined aquifers. *Journal of Hydrology*, *216*(1), 17–31. https://doi.org/10.1016/S0022-1694(98)00275-3

Ataie-Ashtiani, B., Werner, A. D., Simmons, C. T., Morgan, L. K., & Lu, C. (2013). How important is the impact of land-surface inundation on seawater intrusion caused by sea-level rise? *Hydrogeology Journal*, *21*(7), 1673–1677. https://doi.org/10.1007/s10040-013-1021-0

Barbier, E. B., Hacker, S. D., Kennedy, C., Koch, E. W., Stier, A. C., & Silliman, B. R. (2011). The value of estuarine and coastal ecosystem services. *Ecological Monographs*, *81*(2), 169–193. https://doi.org/10.1890/10-1510.1

Barnard, P. L., Erikson, L. H., Foxgrover, A. C., Hart, J. A. F., Limber, P., O'Neill, A. C., et al. (2019). Dynamic flood modeling essential to assess the coastal impacts of climate change. *Scientific Reports*, *9*(1), 1. https://doi.org/10.1038/s41598-019-40742-z

Bolyard, T. H., Hornberger, G. M., Dolan, R., & Hayden, B. P. (1979). Freshwater reserves of mid-Atlantic coast barrier islands. *Environmental Geology*, *3*(1), 1–11. https://doi.org/10.1007/BF02423273

Bonnington, A. C., Jamieson, R. C., Smith, K. A., Oliver, A., Johnston, L. J., LeRoux, N. K., et al. (2023). Impacts of extratropical cyclone fiona on a sensitive coastal lagoon ecosystem. *Limnology & Oceanography*, *68*(12), 2703–2715. https://doi.org/10.1002/lno.12452

Briggs, M. A., Cantelon, J. A., Kurylyk, B. L., Kulongoski, J. T., Mills, A., & Lane, J. W. (2021). Small atoll fresh groundwater lenses respond to a combination of natural climatic cycles and human modified geology. *Science of the Total Environment*, *756*, 143838. https://doi.org/10.1016/j.scitotenv.2020.143838

Brunner, P., & Simmons, C. T. (2012). Hydro geosphere: A fully integrated, physically based hydrological model. *Ground Water*, *50*(2), 170–176. https://doi.org/10.1111/j.1745-6584.2011.00882.x

Bryan, E., Meredith, K. T., Baker, A., Post, V. E. A., & Andersen, M. S. (2016). Island groundwater resources, impacts of abstraction and a drying climate: Rottnest Island, Western Australia. *Journal of Hydrology*, *542*, 704–718. https://doi.org/10.1016/j.jhydrol.2016.09.043

Cantelon, J. A., Guimond, J. A., Robinson, C. E., Michael, H. A., & Kurylyk, B. L. (2022). Vertical saltwater intrusion in coastal aquifers driven by episodic flooding: A review. *Water Resources Research*, *58*(11), e2022WR032614. https://doi.org/10.1029/2022WR032614

Cantelon, J. A., & Kurylyk, B. L. (2023). Applying heat to trace the impacts of storms on coastal morphology and groundwater resources. In *The proceedings of the coastal sediments 2023, New Orleans, LA* (pp. 2468–2481).

Cantelon, J. A., LeRoux, N. K., Mulligan, R. P., Swatridge, L., & Kurylyk, B. L. (2023). Hog Island morphologic and groundwater data [Dataset]. *Borealis*. Retrieved from https://borealisdata.ca/dataset.xhtml?persistentId=doi:10.5683/SP3/KE5YRM

Cardenas, M. B., Bennett, P. C., Zamora, P. B., Befus, K. M., Rodolfo, R. S., Cabria, H. B., & Lapus, M. R. (2015). Devastation of aquifers from tsunami-like storm surge by Supertyphoon Haiyan. *Geophysical Research Letters*, *42*(8), 2844–2851. https://doi.org/10.1002/2015GL063418

Cartwright, N., Baldock, T. E., Nielsen, P., Jeng, D.-S., & Tao, L. (2006). Swash-aquifer interaction in the vicinity of the water table exit point on a sandy beach. *Journal of Geophysical Research: Oceans*, *111*(C9), C09035. https://doi.org/10.1029/2005JC003149

Cartwright, N., & Nielsen, P. (2001). Groundwater dynamics and salinity in beaches. In *The proceedings of coasts and ports* (pp. 441–446).

Chambers, L. G., Osborne, T. Z., & Reddy, K. R. (2013). Effect of salinity-altering pulsing events on soil organic carbon loss along an intertidal wetland gradient: A laboratory experiment. *Biogeochemistry*, *115*(1), 363–383. https://doi.org/10.1007/s10533-013-9841-5

Chesnaux, R., Marion, D., Boumaiza, L., Richard, S., & Walter, J. (2021). An analytical methodology to estimate the changes in fresh groundwater resources with sea-level rise and coastal erosion in strip-island unconfined aquifers: Illustration with Savary Island, Canada. *Hydrogeology Journal*, *29*(3), 1355–1364. https://doi.org/10.1007/s10040-020-02300-0

Claudino-Sales, V., Wang, P., & Horwitz, M. H. (2010). Effect of Hurricane Ivan on coastal dunes of Santa Rosa Barrier Island, Florida: Characterized on the basis of pre- and poststorm LIDAR surveys. *Journal of Coastal Research*, *263*, 470–484. https://doi.org/10.2112/08-1105.1

Davidson, S. G., Hesp, P. A., & Silva, G. M. D. (2020). Controls on dune scarping. *Progress in Physical Geography: Earth and Environment*, *44*(6), 923–947. https://doi.org/10.1177/0309133320932880

Davies, M. (2011). *Geomorphic shoreline classification of Prince Edward island (consulting)* (pp. 1–70). Coldwater Consulting Ltd. Retrieved from http://www.atlanticadaptation.ca

DFO. (2023). MSC50 wind and wave climate hindcast [Dataset]. *Canada: Marine Environmental Data Section Archive, Ecosystem and Oceans Science*. Retrieved from https://meds-sdmm.dfo-mpo.gc.ca

Dietz, S., & Arnold, S. (2021). Atlantic provinces. In F. J. Warren, N. Lulham, & D. S. Lemmen (Eds.), *Chapter 1 in Canada in a changing climate: Regional perspectives report*. Government of Canada.

Dolan, K. (2022). *Hydrodynamic forcing and erosion dynamics on two small islands off the north shore of Prince Edward island: A baseline assessments (Master's Thesis)*. Dalhousie University.

Durán Vinent, O., & Moore, L. J. (2015). Barrier island bistability induced by biophysical interactions. *Nature Climate Change*, *5*(2), 158–162. https://doi.org/10.1038/nclimate2474

Elsayed, S. M., & Oumeraci, H. (2018). Modelling and management of strom-driven saltwater intrusion in freshwater aquifers: The case of near Bremherhaven, Germany. In R. Silva & V. Chavez (Eds.), *Integrating ecosystems in coastal engineering practice (INECEP)*. Puerto Morelos.

Everard, M., Jones, L., & Watts, B. (2010). Have we neglected the societal importance of sand dunes? An ecosystem services perspective. *Aquatic Conservation: Marine and Freshwater Ecosystems*, *10*(4), 476–487. https://doi.org/10.1002/aqc.1114

Fetter, C. W. (1972). Position of the saline water interface beneath oceanic islands. *Water Resources Research*, *8*(5), 1307–1315. https://doi.org/10.1029/WR008i005p01307

Garner, A. J. (2023). Observed increases in North Atlantic tropical cyclone peak intensification rates. *Scientific Reports*, *13*(1), 16299. https://doi.org/10.1038/s41598-023-42669-y

George, E., Lunardi, B., Smith, A., Lehner, J., Wernette, P., & Houser, C. (2021). Short communication: Storm impact and recovery of a beach-dune system in Prince Edward Island. *Geomorphology*, *384*, 107721. https://doi.org/10.1016/j.geomorph.2021.107721

Gheuens, J., Nagabhatla, N., & Perera, E. D. (2019). Disaster-risk, water security challenges and strategies in small island developing states (SIDS). *Water*, *11*(4), 637. https://doi.org/10.3390/w11040637

Ghosh, T., Hajra, R., & Mukhopadhyay, A. (2014). Island erosion and afflicted population: Crisis and policies to handle climate change. In W. Leal Filho, F. Alves, S. Caeiro, & U. Azeiteiro (Eds.), *International perspectives on climate change management*. Springer. https://doi.org/10.1007/978-3-319-04489-7_15

Ghyben, B. W. (1888). *Nota in verband met de voorgenomen put-boring nabij Amsterdam (Notes on the probable results of the proposed well drilling in Amsterdam)* (pp. 8–22). Tijdschrift van het Koninklijk Institunt van Ingeniers.

Gingerich, S. B., Voss, C. I., & Johnson, A. G. (2017). Seawater-flooding events and impact on freshwater lenses of low-lying islands: Controlling factors, basic management and mitigation. *Journal of Hydrology*, *551*, 676–688. https://doi.org/10.1016/j.jhydrol.2017.03.001

Guimond, J. A., & Michael, H. A. (2021). Effects of marsh migration on flooding, saltwater intrusion, and crop yield in coastal agricultural land subject to storm surge inundation. *Water Resources Research*, *57*(2), e2020WR028326. https://doi.org/10.1029/2020WR028326

Habel, S., Fletcher, C. H., Anderson, T. R., & Thompson, P. R. (2020). Sea-level rise induced multi-mechanism flooding and contribution to urban infrastructure failure. *Scientific Reports*, *10*(1), 3796. https://doi.org/10.1038/s41598-020-60762-4

Hapke, C., Brenner, O., Hehre, R., & Reynolds, B. J. (2013). *Coastal change from Hurricane Sandy and the 2012–13 winter storm season—Fire Island* (p. 37). U.S. Geological Survey, Open-File Report No. 2013–1231. Retrieved from http://pubs.usgs.gov/of/2013/1231/

Hay, J. E. (2013). Small island developing states: Coastal systems, global change and sustainability. *Sustainability Science*, *8*(3), 309–326. https://doi.org/10.1007/s11625-013-0214-8

Héquette, A., Ruz, M.-H., Zemmour, A., Marin, D., Cartier, A., & Sipka, V. (2019). Alongshore variability in coastal dune erosion and post-storm recovery, Northern Coast of France. *Journal of Coastal Research*, *88*(1), 25–45. https://doi.org/10.2112/SI88-004.1

Herzberg, A. (1901). Die Wasserversorgung einiger Nordseeb-ider (The water supply on parts of the North Sea coast in Germany). *Journal Gabeleucht Ung Und Wasserversorg Ung*, *44*, 815–819. https://doi.org/10.1007/s11625-013-0214-8

21699011, 2024, 4, Downloaded from https://agupubs.onlinelibrary.wiley.com/doi/10.1029/2023JF007551, Wiley Online Library on [18/06/2024]. See the Terms and Conditions (https://onlinelibrary.wiley.com/terms-and-conditions) on Wiley Online Library for rules of use; OA articles are governed by the applicable Creative Commons License

Hesp, P. A. (2002). Foredunes and blowouts: Initiation, geomorphology and dynamics. In *29th Binghamton geomorphology symposium: Coastal geomorphology* (Vol. 48, pp. 245–268). https://doi.org/10.1016/S0169-555X(02)00184-8
Hesp, P. A. (1988). Morphology, dynamics and internal stratification of some established foredunes in southeast Australia. *Eolian Sediments*, *55*(1), 17–41. https://doi.org/10.1016/0037-0738(88)90088-7
Hesp, P. A., & Smyth, T. A. G. (2016). Jet flow over foredunes. *Earth Surface Processes and Landforms*, *41*(12), 1727–1735. https://doi.org/10.1002/esp.3945
Hesp, P. A., & Walker, I. J. (2022). Coastal dunes. In *Treatise on geomorphology* (pp. 540–591). Elsevier. https://doi.org/10.1016/B978-0-12-818234-5.00220-0
Holding, S., Allen, D., Foster, S., Hsieh, A., Larocque, I., Klassen, J., & Van Pelt, S. C. (2016). Groundwater vulnerability on small islands. *Nature Climate Change*, *6*(12), 1100–1103. https://doi.org/10.1038/nclimate3128
Holding, S., & Allen, D. M. (2015a). From days to decades: Numerical modelling of freshwater lens response to climate change stressors on small low-lying islands. *Hydrology and Earth System Sciences*, *19*(2), 933–949. https://doi.org/10.5194/hess-19-933-2015
Holding, S., & Allen, D. M. (2015b). Wave overwash impact on small islands: Generalised observations of freshwater lens response and recovery for multiple hydrogeological settings. *Journal of Hydrology*, *529*, 1324–1335. https://doi.org/10.1016/j.jhydrol.2015.08.052
Holgate, S. J., Matthews, A., Woodworth, P. L., Rickards, L. J., Tamisiea, M. E., Bradshaw, E., et al. (2013). New data systems and products at the permanent service for mean sea level. *Journal of Coastal Research*, *29*(3), 494–504. https://doi.org/10.2112/JCOASTRES-D-1200175.1
Holt, T., Greskowiak, J., Seibert, S. L., & Massmann, G. (2019). Modeling the evolution of a freshwater lens under highly dynamic conditions on a currently developing barrier island. *Geofluids*, *2019*, 15. https://doi.org/10.1155/2019/9484657
Housego, R., Raubenheimer, B., Elgar, S., Cross, S., Legner, C., & Ryan, D. (2021). Coastal flooding generated by ocean wave- and surge-driven groundwater fluctuations on a sandy barrier island. *Journal of Hydrology*, *603*, 126920. https://doi.org/10.1016/j.jhydrol.2021.126920
Houser, C. (2013). Alongshore variation in the morphology of coastal dunes: Implications for storm response. In *Coastal geomorphology and restoration 44th Binghamton geomorphology symposium* (Vol. 199, pp. 48–61). https://doi.org/10.1016/j.geomorph.2012.10.035
Houser, C., & Hamilton, S. (2009). Sensitivity of post-hurricane beach and dune recovery to event frequency. *Earth Surface Processes and Landforms*, *34*(5), 613–628. https://doi.org/10.1002/esp.1730
Houser, C., Hapke, C., & Hamilton, S. (2008). Controls on coastal dune morphology, shoreline erosion and barrier island response to extreme storms. *Geomorphology*, *100*(3), 223–240. https://doi.org/10.1016/j.geomorph.2007.12.007
Houser, C., Wernette, P., Rentschlar, E., Jones, H., Hammond, B., & Trimble, S. (2015). Post-storm beach and dune recovery: Implications for barrier island resilience. *Geomorphology*, *234*, 54–63. https://doi.org/10.1016/j.geomorph.2014.12.044
Huizer, S., Essink, G. H. P., & Bierkens, M. F. P. (2016). Fresh groundwater resources in a large sand replenishment. *Hydrology and Earth System Sciences*, *20*(8), 3149–3166. https://doi.org/10.5194/hess-20-3149-2016
Huizer, S., Karaoulis, M. C., Oude Essink, G. H. P., & Bierkens, M. F. P. (2017). Monitoring and simulation of salinity changes in response to tide and storm surges in a sandy coastal aquifer system. *Water Resources Research*, *53*(8), 6487–6509. https://doi.org/10.1002/2016WR020339
IPCC. (2023). Climate change 2023: Synthesis report. In Core Writing Team, H. Lee, & J. Romero (Eds.), *Contribution of working groups I, II and III to the sixth assessment report of the intergovernmental panel on climate change* (pp. 35–115). IPCC. https://doi.org/10.59327/IPCC/AR6-9789291691647
Jardine, D. (2022). Prince edward island annual climate summary 2021 [Dataset]. *Centre for Climate Change and Adaptation (Climate Centre)*. Retrieved from https://weatherspark.com/y/21252/Average-Weather-in-Prince-Edward-Canada-Year-Round
Jiao, J., & Post, V. E. A. (2019). *Coastal Hydrogeology*. Cambridge University Press. https://doi.org/10.1017/9781139344142
Kamphuis, W. J. (2020). Chapter 4: Long-term wave analysis. In *Introduction to coastal engineering and management* (3rd ed., Vol. 48). World Scientific Publishing Company.
Kirsh. (2009). *Groundwater geophysics: A tool for hydrogeology*. Springer.
Klein, Y. L., Osleeb, J. P., & Viola, M. R. (2004). Tourism-generated earnings in the coastal zone: A regional analysis. *Journal of Coastal Research*, *20*(4), 1080–1088. https://doi.org/10.2112/003-0018.1
Lee, W. D., Yoo, Y. J., Jeong, Y. M., & Hur, D. S. (2019). Experimental and numerical analysis on hydraulic characteristics of coastal aquifers with seawall. *Water*, *11*(11), 2343. https://doi.org/10.3390/w11112343
LeRoux, N. K., Frey, S. K., Lapen, D. R., Guimond, J. A., & Kurylyk, B. L. (2023). Mega-tidal and surface flooding controls on coastal groundwater and saltwater intrusion within agricultural dikelands. *Water Resources Research*, *59*(11), e2023WR035054. https://doi.org/10.1029/2023WR035054
LeRoux, N. K., Pavlovskii, I., O'Sullivan, A. M., Mulligan, R. P., Bonnington, A. C., & Kurylyk, B. K. (2024). Morphodynamics of a composite sand-cobble beach in response to extratropical cyclone Fiona and seasonal wave variability. *Science of the Total Environment*, *916*, 170077. https://doi.org/10.1016/j.scitotenv.2024.170077
Liebowitz, D. M., Nielsen, K. J., Dugan, J. E., Morgan, S. G., Malone, D. P., Largier, J. L., et al. (2016). Ecosystem connectivity and trophic subsidies of sandy beaches. *Ecosphere*, *7*(10), e01503. https://doi.org/10.1002/ecs2.1503
Liu, J., & Tokunaga, T. (2019). Future risks of tsunami-induced seawater intrusion into unconfined coastal aquifers: Insights from numerical simulations at Niijima Island, Japan. *Water Resources Research*, *55*(12), 10082–10104. https://doi.org/10.1029/2019WR025386
Luijendijk, A., Hagenaars, G., Ranasinghe, R., Baart, F., Donchyts, G., & Aarninkhof, S. (2018). The state of the world's beaches. *Scientific Reports*, *8*(1), 6641. https://doi.org/10.1038/s41598-018-24630-6
MacDonald, K. (2014). *Modeling present and future physical coastal vulnerability to climate change: North shore, Prince Edward island [Master's thesis, University of Waterloo]*. UWSpace. Retrieved from http://hdl.handle.net/10012/8482
Marmoush, R. Y., & Mulligan, R. P. (2020). A three-dimensional laboratory investigation of beach morphology change during a storm event. *Geomorphology*, *363*, 107224. https://doi.org/10.1016/j.geomorph.2020.107224
Marsooli, R., Lin, N., Emanuel, K., & Feng, K. (2019). Climate change exacerbates hurricane flood hazards along US Atlantic and Gulf Coasts in spatially varying patterns. *Nature Communications*, *10*(1), 3785. https://doi.org/10.1038/s41467-019-11755-z
Masselink, G., Castelle, B., Scott, T., Dodet, G., Suanez, S., Jackson, D., & Floc'h, F. (2016). Extreme wave activity during 2013/2014 winter and morphological impacts along the Atlantic coast of Europe. *Geophysical Research Letters*, *45*(5), 1064–1071. https://doi.org/10.1002/2015GL067492
Masterson, J. P., Fienen, M. N., Thieler, E. R., Gesch, D. B., Gutierrez, B. T., & Plant, N. G. (2014). Effects of sea-level rise on barrier island groundwater system dynamics – Ecohydrological implications. *Ecohydrology*, *7*(3), 1064–1071. https://doi.org/10.1002/eco.1442
Mathew, S., Davidson-Arnott, R. G. D., & Ollerhead, J. (2010). Evolution of a beach–dune system following a catastrophic storm overwash event: Greenwich Dunes, Prince Edward Island, 1936–2005. *Canadian Journal of Earth Sciences*, *47*(3), 273–290. https://doi.org/10.1139/E09-078
McCann, S. B. (1972). Reconnaissance survey of Hog island, Prince Edward Island. *Atlantic Geology*, *8*(3), 107–113. https://doi.org/10.4138/1416

21699011, 2024, 4, Downloaded from https://agupubs.onlinelibrary.wiley.com/doi/10.1029/2023JF007551, Wiley Online Library on [18/06/2024]. See the Terms and Conditions (https://onlinelibrary.wiley.com/terms-and-conditions) on Wiley Online Library for rules of use; OA articles are governed by the applicable Creative Commons License

McDonald, K. S., Hobday, A. J., Thompson, P. A., Lenton, A., Stephenson, R. L., Mapstone, B. D., et al. (2019). Proactive, reactive, and inactive pathways for scientists in a changing world. *Earth's Future*, *7*(2), 60–73. https://doi.org/10.1029/2018EF000990

McGranahan, G., Balk, D., & Anderson, B. (2007). The rising tide: Assessing the risks of climate change and human settlements in low elevation coastal zones. *Environment and Urbanization*, *19*(1), 17–37. https://doi.org/10.1177/0956247807076960

McNamara, D. E., & Lazarus, E. D. (2018). Barrier islands as coupled human–landscape systems. In L. J. Moore & A. B. Murray (Eds.), *Barrier dynamics and response to changing climate* (pp. 363–383). Springer International Publishing. https://doi.org/10.1007/978-3-319-68086-6_12

MCPEI. (2023). HOBOLink Hog island-MCPEI [Dataset]. *Climate*. Retrieved from https://www.hobolink.com/p/eff9c129a08a05574e2e25dd74d4ec41

Michael, H. A., Post, V. E. A., Wilson, A. M., & Werner, A. D. (2017). Science, society, and the coastal groundwater squeeze. *Water Resources Research*, *53*(4), 2610–2617. https://doi.org/10.1002/2017WR020851

Mulligan, R. P., Swatridge, L., Cantelon, J. A., Kurylyk, B. L., George, K., & Houser, C. (2023). Local and remote storm surge contributions to total water levels in the Gulf of St. Lawrence during Hurricane Fiona. *Journal of Geophysical Research- Oceans*, *128*(8), e2023JC019910. https://doi.org/10.1029/2023JC019910

Nayar, K. G., Sharqawy, M. H., Banchik, L. D., & Lienhard, J. H. (2016). Thermophysical properties of seawater: A review and new correlations that include pressure dependence. *Desalination*, *390*, 1–24. https://doi.org/10.1016/j.desal.2016.02.024

Nielsen, P. (1990). Tidal dynamics of the water table in beaches. *Water Resources Research*, *26*(9), 2127–2134. https://doi.org/10.1029/WR026i009p02127

Nielsen, P., & Hanslow, D. J. (1991). Wave runup distributions on natural beaches. *Journal of Coastal Research*, *7*(4), 1139–1152. Retrieved from http://www.jstor.org/stable/4297933

Nordio, G., Frederiks, R., Hingst, M., Carr, J., Kirwan, M., Gedan, K., et al. (2023). Frequent storm surges affect the groundwater of coastal ecosystems. *Geophysical Research Letters*, *50*(1), e2022GL100191. https://doi.org/10.1029/2022GL100191

Nunn, P. D., Klock, C., & Duvat, V. (2021). Seawalls as maladaptations along island coasts. *Ocean & Coastal Management*, *205*, 105554. https://doi.org/10.1016/j.ocecoaman.2021.105554

Oberle, F. K. J., Swarzenski, P. W., & Storlazzi, C. D. (2017). Atoll groundwater movement and its response to climatic and sea level fluctuations. *Water*, *9*(9), 650. https://doi.org/10.3390/w9090650

Paldor, A., Frederiks, R. S., & Michael, H. A. (2022). Dynamic steady state in coastal aquifers is driven by multi-scale cyclical processes, controlled by aquifer storativity. *Geophysical Research Letters*, *49*(11), 2701. https://doi.org/10.1029/2022GL098599

Paldor, A., Stark, N., Florence, M., Raubenheimer, B., Elgar, S., Housego, R., et al. (2022). Coastal topography and hydrogeology control critical groundwater gradients and potential beach surface instability during storm surges. *Hydrology and Earth System Sciences*, *26*(23), 5987–6002. https://doi.org/10.5194/hess-26-5987-2022

Paprotny, D., Terefenko, P., Giza, A., Czapliński, P., & Vousdoukas, M. I. (2021). Future losses of ecosystem services due to coastal erosion in Europe. *Science of the Total Environment*, *760*, 144310. https://doi.org/10.1016/j.scitotenv.2020.144310

Parkinson, R. W. (2021). Speculation on the role of sea-level rise in the tragic collapse of the surfside condominium (Miami Beach, Florida U.S. A.) was a bellwether moment for coastal zone management practitioners. *Ocean & Coastal Management*, *215*, 105968. https://doi.org/10.1016/j.ocecoaman.2021.105968

Parks Canada. (2021). *Feasibility assessment on the creation of a national park reserve in Pituamkek (Hog Island Sandhills)*. Parks Canada. Retrieved from https://parks.canada.ca/pn-np/cnpn-cnnp/pituamkek

Pasch, R. J., Reinhart, B. J., & Alaka, L. (2023). *Hurricane Fiona (No. AL072022)*. National Hurricane Center.

Pavlovskii, I., Jiang, Y., Danielescu, S., & Kurylyk, B. L. (2023). Influence of precipitation event magnitude on baseflow and coastal nitrate export for Prince Edward Island, Canada. *Hydrological Processes*, *37*(5), e14892. https://doi.org/10.1002/hyp.14892

Pelling, M., & Uitto, J. I. (2011). Small island developing states: Natural disaster vulnerability and global change. *Global Environmental Change Part B: Environmental Hazards*, *3*(2), 49–62. https://doi.org/10.3763/ehaz.2001.0306

Planet Team. (2017). Planet application program interface: In space for life on Earth [Software]. *San Francisco, CA*. Retrieved from https://api.planet.com

Post, V. E. A., & Houben, G. J. (2017). Density-driven vertical transport of saltwater through the freshwater lens on the island of Baltrum (Germany) following the 1962 storm flood. *Investigation of Coastal Aquifers*, *551*, 689–702. https://doi.org/10.1016/j.jhydrol.2017.02.007

Priestas, A. M., & Fagherazzi, S. (2010). Morphological barrier island changes and recovery of dunes after Hurricane Dennis, St. George Island, Florida. *Geomorphology*, *114*(4), 614–626. https://doi.org/10.1016/j.geomorph.2009.09.022

Rakhimbekova, S., Power, C., O'Carroll, D. M., & Robinson, C. E. (2023). Potential for shoreline recession to accelerate discharge of groundwater pollutants to coastal waters. *Water Resources Research*, *59*(6), e2022WR034230. https://doi.org/10.1029/2022WR034230

Richardson, C. M., Davis, K. L., Ruiz-González, C., Guimond, J. A., Micheal, H. A., Paldor, A., et al. (2024). The impacts of climate change on coastal groundwater. *Nature Reviews Earth & Environment*, *5*(2), 1–20. https://doi.org/10.1038/s43017-023-00500-2

Robins, N. S. (2013). A review of small island hydrogeology: Progress (and setbacks) during the recent past. *The Quarterly Journal of Engineering Geology and Hydrogeology*, *46*(2), 157–165. https://doi.org/10.1144/qjegh2012-063

Roelvink, D., Reniers, A. J. H. M., van Dongeren, A. P., Van Thiel de Vries, J., Lescinski, J., & McCall, R. (2010). *XBeach model description and manual*. Unesco-IHE Institute for Water Education, Deltares and Delft University of Tecnhology.

Röper, T., Greskowiak, J., Freund, H., & Massmann, G. (2013). Freshwater lens formation below juvenile dunes on a barrier island (Spiekeroog, Northwest Germany). *Estuarine, Coastal and Shelf Science*, *121–122*, 40–50. https://doi.org/10.1016/j.ecss.2013.02.004

Santos, I. R., Chen, X., Lecher, A. L., Sawyer, A. H., Moosdorf, N., Rodellas, V., et al. (2021). Submarine groundwater discharge impacts on coastal nutrient biogeochemistry. *Nature Reviews Earth & Environment*, *2*(5), 307–323. https://doi.org/10.1038/s43017-021-00152-0

Schlacher, T. A., Schoeman, D. S., Dugan, J., Lastra, M., Jones, A., Scapini, F., & McLachlan, A. (2008). Sandy beach ecosystems: Key features, sampling issues, management challenges and climate change impacts. *Marine Ecology*, *29*(1), 70–90. https://doi.org/10.1111/j.1439-0485.2007.00204.x

Schneider, J. C., & Kruse, S. E. (2003). A comparison of controls on freshwater lens morphology of small carbonate and siliciclastic islands: Examples from barrier islands in Florida, USA. *Journal of Hydrology*, *284*(1), 253–269. https://doi.org/10.1016/j.jhydrol.2003.08.002

Schneider, J. C., & Kruse, S. E. (2006). Assessing selected natural and anthropogenic impacts on freshwater lens morphology on small barrier Islands: Dog Island and St. George Island, Florida, USA. *Hydrogeology Journal*, *14*(1), 131–145. https://doi.org/10.1007/s10040-005-0442-9

Seibert, S. L., Böttcher, M. E., Waska, H., Holt, T., Pollmann, T., Greskowiak, J., & Massmann, G. (2021). Hydrogeochemistry of near-surface groundwater on a developing barrier island (Spiekeroog, Germany): The role of inundation, season and vegetation. *Journal of Hydrology*, *597*, 126139. https://doi.org/10.1016/j.jhydrol.2021.126139

21699011, 2024, 4, Downloaded from https://agupubs.onlinelibrary.wiley.com/doi/10.1029/2023JF007551, Wiley Online Library on [18/06/2024]. See the Terms and Conditions (https://onlinelibrary.wiley.com/terms-and-conditions) on Wiley Online Library for rules of use; OA articles are governed by the applicable Creative Commons License

Sherwood, C. R., Ritchie, A. C., Over, J.-S. R., Kranenburg, C. J., Warrick, J. A., Brown, J. A., et al. (2023). Sound-side inundation and seaward erosion of a barrier island during hurricane landfall. *Journal of Geophysical Research: Earth Surface*, *128*(1), e2022JF006934. https://doi.org/10.1029/2022JF006934

Sopkin, K. L., Stockdon, H. F., Doran, K. S., Plant, N. G., Morgan, K. L. M., Guy, K. K., & Smith, K. E. L. (2014). Hurricane Sandy: Observations and analysis of coastal change (Report No. 2014–1088), Reston, VA (p. 64). https://doi.org/10.3133/ofr20141088

Stanic, S., LeRoux, N. K., Paldor, A., Mohammed, A. A., Michael, H. A., & Kurylyk, B. L. (2024). Saltwater intrusion into a confined island aquifer driven by erosion, changing recharge, sea-level rise, and coastal flooding. *Water Resources Research*, *60*(1), e2023WR036394. https://doi.org/10.1029/2023WR036394

Storlazzi, C. D., Gingerich, S. B., van Dongeren, A., Cheriton, O. M., Swarzenski, P. W., Quataert, E., et al. (2018). Most atolls will be uninhabitable by the mid-21st century because of sea-level rise exacerbating wave-driven flooding. *Science Advances*, *4*(4), eaap9741. https://doi.org/10.1126/sciadv.aap9741

Tackley, H. A., Kurylyk, B. L., Lake, C. B., Lapen, D. R., & van Proosdij, D. (2023). Impacts of repeated coastal flooding on soil and groundwater following managed dike realignment. *Science of the Total Environment*, *893*, 164957. https://doi.org/10.1016/j.scitotenv.2023.164957

Taniguchi, M., Dulai, H., Burnett, K. M., Santos, I. R., Sugimoto, R., Stieglitz, T., et al. (2019). Submarine groundwater discharge: Updates on its measurement techniques, geophysical drivers, magnitudes, and effects. *Frontiers in Environmental Science*, *7*, 141. https://doi.org/10.3389/fenvs.2019.00141

Terry, J. P., & Falkland, A. C. (2010). Responses of atoll freshwater lenses to storm-surge overwash in the Northern Cook Islands. *Hydrogeology Journal*, *18*(3), 749–759. https://doi.org/10.1007/s10040-009-0544-x

Threndyle, R. E., Jamieson, R. C., Kennedy, G., Lake, C. B., & Kurylyk, B. L. (2022). Future inundation of coastal on-site wastewater treatment systems in a region with pronounced sea-level rise. *Journal of Hydrology*, *614*, 128548. https://doi.org/10.1016/j.jhydrol.2022.128548

Toimil, A., Losada, I. J., Nicholls, R. J., Dalrymple, R. A., & Stive, M. J. F. (2020). Addressing the challenges of climate change risks and adaptation in coastal areas: A review. *Coastal Engineering*, *156*, 103611. https://doi.org/10.1016/j.coastaleng.2019.103611

UNESCO-IHP & UNEP. (2016). *Transboundary Aquifers and Groundwater Systems of Small Island Developing States: Status and Trends, Summary for Policy Makers*. United Nations Environment Programme (UNEP). Retrieved from https://unesdoc.unesco.org/ark:/48223/pf0000244912

Vacher, H. L. (1988). Ground water in barrier islands: Theoretical analysis and evaluation of the unequal-sea level problem. *Journal of Coastal Research*, *4*(1), 139–148. Retrieved from https://www.jstor.org/stable/4297381

Vasseur, L., & Catto, N. R. (2008). Chapter 4: Atlantic Canada. In *From impacts to adaptation: Canada in a changing climate* (pp. 119–170). Government of Canada.

Vithanage, M., Meththika, E. P., Villholth, K. G., & Jensen, K. H. (2012). The effects of the 2004 tsunami on a coastal aquifer in Sri Lanka. *Ground Water*, *50*(5), 704–714. https://doi.org/10.1111/j.1745-6584.2011.00893.x

Vitousek, S., Barnard, P. L., Fletcher, C. H., Frazer, N., Erikson, L., & Storlazzi, C. D. (2017). Doubling of coastal flooding frequency within decades due to sea-level rise. *Scientific Reports*, *7*(1), 1399. https://doi.org/10.1038/s41598-017-01362-7

Vousdoukas, M., Mentaschi, L., Voukouvalas, E., Verlaan, M., Jevrejeva, S., Jackson, L. P., & Feyen, L. (2018). Global probabilistic projections of extreme sea levels show intensification of coastal flood hazard. *Nature Communications*, *9*(1), 2360. https://doi.org/10.1038/s41467-018-04692-w

Vousdoukas, M., Ranasinghe, R., Mentaschi, L., Plomaritis, T. A., Athanasiou, P., Luijendijk, A., & Feyen, L. (2020). Sandy coastlines under threat of erosion. *Nature Climate Change*, *10*(3), 260–263. https://doi.org/10.1038/s41558-020-0697-0

Wang, X., & Du, J. (2016). Submarine groundwater discharge into typical tropical lagoons: A case study in eastern Hainan island, China. *Geochemistry, Geophysics, Geosystems*, *17*(11), 4366–4382. https://doi.org/10.1002/2016GC006502

Werner, A. D., Bakker, M., Post, V. E. A., Vandenbohede, A., Lu, C., Ataie-Ashtiani, B., et al. (2013). Seawater intrusion processes, investigation and management: Recent advances and future challenges. *Advances in Water Resources*, *51*, 3–26. https://doi.org/10.1016/j.advwatres.2012.03.004

Wernette, P., Houser, C., & Bishop, M. P. (2016). An automated approach for extracting barrier island morphology from digital elevation models. *Geomorphology*, *262*, 1–7. https://doi.org/10.1016/j.geomorph.2016.02.024

White, I., & Falkland, T. (2010). Management of freshwater lenses on small Pacific islands. *Hydrogeology Journal*, *18*(1), 227–246. https://doi.org/10.1007/s10040-009-0525-0

Wolinsky, M. A., & Murray, A. B. (2009). A unifying framework for shoreline migration: 2. Application to wave-dominated coasts. *Journal of Geophysical Research*, *114*(F1), F01009. https://doi.org/10.1029/2007JF000856

Wong, V. N. L., Johnston, S. G., Burton, E. D., Hirst, P., Sullivan, L. A., Bush, R. T., & Blackford, M. (2015). Seawater inundation of coastal floodplain sediments: Short-term changes in surface water and sediment geochemistry. *Chemical Geology*, *398*, 32–45. https://doi.org/10.1016/j.chemgeo.2015.01.016

Wu, L., Zhao, H., Wang, C., Cao, J., & Liang, J. (2022). Understanding of the effect of climate change on tropical cyclone intensity: A review. *Advances in Atmospheric Sciences*, *39*(2), 205–221. https://doi.org/10.1007/s00376-021-1026-x

Yang, Z., Zhou, Y., Wenninger, J., Uhlenbrook, S., & Wan, L. (2015). Simulation of groundwater-surface water interactions under different land use scenarios in the Bulang catchment. *Northwest China. Water*, *7*(11), 5959–5985. https://doi.org/10.3390/w7115959

Yu, X., Yang, J., Graf, T., Koneshloo, M., O'Neal, M. A., & Michael, H. A. (2016). Impact of topography on groundwater salinization due to ocean surge inundation. *Water Resources Research*, *52*(8), 5794–5812. https://doi.org/10.1002/2016WR018814

Zhang, Y., Li, L., Erler, D. V., Santos, I., & Lockington, D. (2016). Effects of alongshore morphology on groundwater flow and solute transport in a nearshore aquifer: 3-D nearshore groundwater flow and solute transport. *Water Resources Research*, *52*(2), 990–1008. https://doi.org/10.1002/2015WR017420

References From the Supporting Information

Aarhus Geosoftware. (2023). Aarhus SPIA 3.2.1 [Software]. *Aarhus Geosoftware*. Retrieved from https://www.aarhusgeosoftware.dk/download-aarhus-workbench

Cantelon, J. A., Robinson, C. E., & Kurylyk, B. L. (2023). Morphologic, atmospheric, and oceanic drivers cause multi-temporal saltwater intrusion on a remote, sand island. *Water Resources Research*, *59*(10), e2023WR035820. https://doi.org/10.1029/2023WR035820

DFO. (2023). *Marine Environmental Data Section Archive*. Ecosystem and Oceans Science, Department of Fisheries and Oceans Canada. Retrieved from https://meds-sdmm.dfo-mpo.gc.ca/

21699011, 2024, 4, Downloaded from https://agupubs.onlinelibrary.wiley.com/doi/10.1029/2023JF007551, Wiley Online Library on [18/06/2024]. See the Terms and Conditions (https://onlinelibrary.wiley.com/terms-and-conditions) on Wiley Online Library for rules of use; OA articles are governed by the applicable Creative Commons License